Ann Thorac Surg
2008;85:1430–2

Novel Germline Mutation: *EGFR* V843I in Patient With Multiple Lung Adenocarcinomas and Family Members With Lung Cancer

Koei Ikeda, MD, PhD, Hiroaki Nomori, MD, PhD, Takeshi Mori, MD, PhD, Jiichiro Sasaki, MD, PhD, and Toshiaki Kobayashi, MD, PhD

Department of Thoracic Surgery, Graduate School of Medical Sciences, Kumamoto University, Department of Respiratory Medicine, Kumamoto University Hospital, Kumamoto and Department of Assistive Diagnostic Technology, National Cancer Center Hospital, Tokyo, Japan

A novel germline transmission of the epidermal growth factor receptor (EGFR) mutation V843I in a family with multiple members with lung cancer is reported. The proband was a 70-year-old woman with multiple adenocarcinomas who exhibited secondary *EGFR* mutations, either L858R or L861Q, in the specimens of resected tumors, in addition to a germline *EGFR* V843I mutation. These observations suggest that the germline *EGFR* V843I mutation might have altered EGFR signaling in the multicentric development of adenocarcinoma, bronchoalveolar carcinoma, and atypical adenomatous hyperplasia and also might have had a role in the development of lung cancer in multiple members of her family.

(Ann Thorac Surg 2008;85:1430–2)

FEATURE ARTICLES

Recent advances in high-resolution computed tomography (CT) have increased the detection of multicentric adenocarcinoma (AD) [1]. However, the cause of multicentric development of lung AD is unknown. Recently a germline epidermal growth factor receptor (EGFR) mutation, T790M, found to be a drug-resistant mutation of EGFR tyrosine kinase inhibitors, was reported in one family that included several patients with lung cancer [2]. We report a novel germline mutation, *EGFR* V843I, in a woman with multiple lung ADs and family members with lung cancer.

The patient was a 70-year-old woman. Her father and a brother (I-1 and II-1, respectively; Fig 1) had died of lung cancer. Her brother also had stomach and prostate gland cancer. In the case patient, multiple pulmonary nodules were demonstrated on CT scans obtained during a routine medical examination (Fig 2). A CT-guided needle biopsy of the bilateral nodules revealed AD. Right upper and middle lobectomies were performed, followed by wedge resection of the left pulmonary nodules 2 months later. Pathologic examination revealed 3 ADs (Figs 2A–C), 4 bronchioloalveolar carcinomas (BACs) (Fig 2D), and 3 lesions of atypical adenomatous hyperplasia (AAH) (Fig 2E). The AD had metastasized to the lymph nodes of the right upper lobe. We classified AD in the posterior segment of the right upper lobe (Fig 2B) as T1N1M0, stage IIA, because the nodule was the largest and the pathologic findings showed intratumoral lymphatic invasion. The other resected tumors were classified as T1N0M0, stage IA. The patient refused adjuvant chemotherapy. She has been alive without recurrence for 8 months after surgery.

DNA extraction and direct sequencing were performed by SRL Laboratory Inc, Tokyo, Japan. DNA was extracted from formalin-fixed, paraffin-embedded specimens of three resected ADs (Figs 2A-C), one BAC (Fig 2D), and one AAH (Fig 2E). The tumor cells were microscopically dissected from their 5-μm sections for DNA extraction. Direct sequencing from *EGFR* exon 18, exon19, exon 20, and exon 21 was performed. In addition, mutation analyses were performed on resected adjacent healthy lung tissue and peripheral blood mononuclear cells. After obtaining written informed consent from family members, germline mutations in the peripheral blood mononuclear cells were analyzed in her two brothers (II-2 and II-5; Fig 1) and one sister (II-3; Fig 1), none of whom had lung cancer.

Specimens from all five tumors examined, healthy lung tissue, and peripheral blood mononuclear cells from the patient exhibited the *EGFR* V843I mutation (Figs 3a, c, and e) in exon 21 of the *EGFR* gene. In addition, *EGFR* L861Q (Fig 3b) was detected in ADs in the apical segment of the right upper lobe (Fig 2A) and in the left upper lobe (Fig 2C), and *EGFR* L858R (Fig 3d) in AD in the posterior segment of the right upper lobe (Fig 2B), BAC in the lateral segment of the right middle lobe (Fig 2D), and AAH in the apical anterior segment of the left upper lobe (Fig 2E) (Table 1). These mutations were not detected in the healthy lung tissue and peripheral blood mononu-

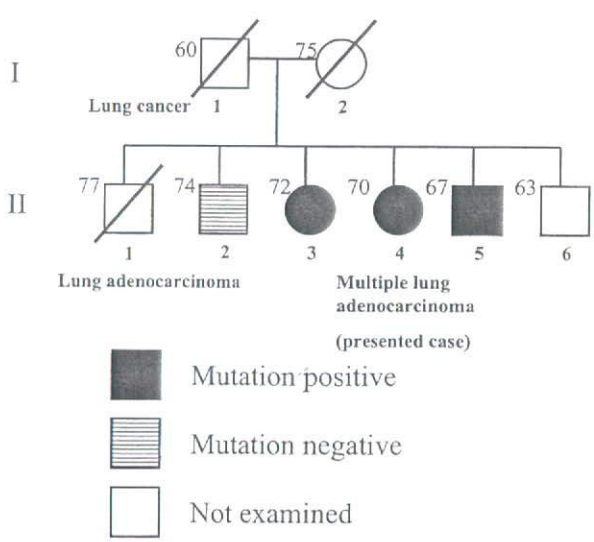

Fig 1. Pedigree of family of case patient (II-4). Boxes and circles indicate males and females, respectively; numbers at left above indicate age at death or time of mutation analysis; and oblique line shows deceased family members.

Accepted for publication Oct 2, 2007.

Address correspondence to Dr Nomori, Department of Thoracic Surgery, Graduate School of Medical Sciences, Kumamoto University, 1-1-1 Honjo, Kumamoto, 860-8556, Japan; e-mail: hnomori@qk9.so-net.ne.jp.

0003-4975/08/$34.00
doi:10.1016/j.athoracsur.2007.10.012

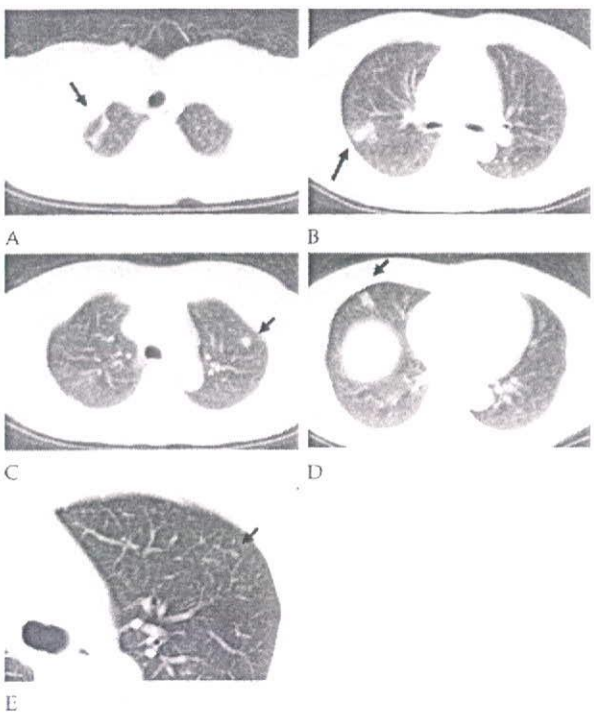

Fig 2. Findings at computed tomography. (A) Adenocarcinoma (arrow) in apical segment of right upper lobe. (B) Adenocarcinoma (arrow) in posterior segment of right upper lobe. (C) Adenocarcinoma (arrow) in left upper lobe. (D) Bronchioloalveolar carcinoma (arrow) in right middle lobe. (E) Atypical adenomatous hyperplasia (arrow) in left upper lobe.

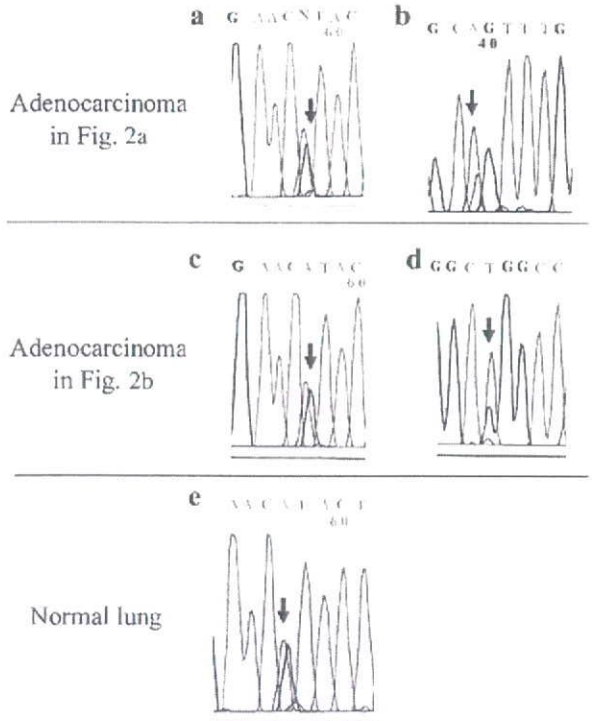

Fig 3. Nucleotide sequence tracings. Tracings (a), (c) and (e) show G to A mutation, which represents germline V843I mutation in EGFR gene. Tracing (b) shows A to T mutation, which represents L861Q mutation in tumor (reverse sequence). Tracing (d) shows T to G mutation, which represents L858R mutation in tumor (reverse sequence).

clear cells. Of her three affected family members, two (II-3 and II-5; Fig 1) had the germline V843I mutation and one (II-2; Fig 1) did not. All mutations were harbored in exon 21 of the *EGFR* gene, and there were no mutations of exon 18, 19, or 20 in any specimens examined.

Comment

Frequent detection of the *EGFR* mutation in lung ADs with BAC features has been reported [3]. Recently, the possibility of an important role of the *EGFR* mutation in the carcinogenesis of lung AD has also been suggested. Tang and colleagues [4] showed that the *EGFR* mutation is frequently present in the normal epithelium of patients with *EGFR* mutant lung AD and suggested that the *EGFR* mutation might be a very early event in the pathogenesis of lung AD. Ji and colleagues [5] demonstrated a close relationship between the *EGFR* mutation and carcinogenesis of lung AD in experiments in transgenic mice.

The *EGFR* V843I mutation has been reported in a patient with lung AD who exhibited a partial response to therapy with gefitinib (Iressa; AstraZeneca Pharmaceuticals LP, Willmington, Delaware) [6] and in a patient with bile duct AD [7]. Our case patient had a germline *EGFR* V843I mutation and additional mutations L861Q and L858R in all five tumor specimens examined. Knudson [8] proposed the two-hit theory of tumor development, that is, that tumors can develop from healthy tissue with congenital first mutations following acquisition of second mutations. We speculate that multifocal development of

Table 1. EGFR Mutations in Examined Tumor Specimens

Pedigree Position and Specimen	EGFR Mutation 1	EGFR Mutation 2
II-4 (case patient)		
AD in S1	Exon 21 V843I	Exon 21 L861Q
AD in S2	Exon 21 V843I	Exon 21 L858R
AD in S3	Exon 21 V843I	Exon 21 L861Q
BAC in S4	Exon 21 V843I	Exon 21 L858R
AAH in S3	Exon 21 V843I	Exon 21 L858R
Healthy lung tissue	Exon 21 V843I	None
Peripheral blood cells	Exon 21 V843I	None
II-2 (brother of case patient)		
Peripheral blood cells	None	None
II-3 (sister of case patient)		
Peripheral blood cells	Exon 21 V843I	None
II-5 (brother of case patient)		
Peripheral blood cells	Exon 21 V843I	None

AD = adenocarcinoma; AAH = atypical adenomatous hyperplasia; S1 = apical segment of right upper lobe; S2 = posterior segment of right upper lobe; S3 = apical anterior segment of left upper lobe; S4 = lateral segment of right middle lobe.

AD, BAC, and AAH in the case patient might have occurred as a result of second-hit mutations L861Q and L858R in the setting of a germline V843I mutation.

However, the effects of the *EGFR* V843I mutation on EGFR signaling and the molecular importance of the double mutation on *EGFR* exon 21 are unknown. The patient's father and a brother had died of lung cancer. However, another brother and a sister, each of whom had germline *EGFR* V843I mutation, have not developed lung cancer despite being almost 70 years old. The role of germline *EGFR* V843I mutation in multifocal lung carcinogenesis and the familial occurrence of lung cancer in the case patient are still unclear. In vitro experiments are needed to clarify the effects of *EGFR* V843I mutation on EGFR signaling, as is accumulation of clinical cases to determine the role of germline *EGFR* mutation in lung carcinogenesis.

References

1. Zwirewich CV, Miller RR, Muller NL. Multicentric adenocarcinoma of the lung: CT-pathologic correlation. Radiology 1990;176:185–90.
2. Bell DW, Gore I, Okimoto RA, et al. Inherited susceptibility to lung cancer may be associated with the T790M drug resistance mutation in EGFR. Nat Genet 2005;37:1315–6.
3. Blons H, Côté JF, Le Corre D, et al. Epidermal growth factor receptor mutation in lung cancer is linked to bronchioloalveolar differentiation. Am J Surg Pathol 2006;30:1309–15.
4. Tang X, Shigematsu H, Bekele N, et al. EGFR tyrosine kinase domain mutations are detected in histologically normal respiratory epithelium in lung cancer patients. Cancer Res 2005;65:7568–72.
5. Ji H, Li D, Chen L, et al. The impact of human EGFR kinase domain mutations on lung tumorigenesis and in vivo sensitivity to EGFR-targeted therapies. Cancer Cells 2006;9:485–95.
6. Shih J-Y, Gow C-H, Yu C-J, et al. Epidermal growth factor receptor mutation in needle biopsy/aspiration samples predicts response to gefitinib therapy and survival of patients with advanced non–small cell lung cancer. Int J Cancer 2006;118:963–9.
7. Leone F, Cavalloni G, Pignochino Y, et al. Somatic mutation of epidermal growth factor recepter in bile duct and gallbladder carcinoma. Clin Cancer Res 2006;12:1680–5.
8. Knudson AG Jr. Overview: genes that predispose to cancer. Mutat Res 1991;247:185–90.

FEATURE ARTICLES

Pseudocavitating Bronchioloalveolar Carcinoma Followed Over a Decade

Jason P. Shaw, MD, Pablo A. Bejarano, MD, and Richard J. Thurer, MD

Department of Surgery, Division of Cardiothoracic Surgery, and Department of Pathology, University of Miami Miller School of Medicine, Miami, Florida

A 38-year-old woman with bronchioloalveolar carcinoma (BAC) had a slow-growing cavitary nodule for nearly a decade. When she was hospitalized because of pneumonia 9 years earlier, a chest computed tomography scan showed a 1.5-cm cavitary right upper lobe nodule. At 1, 3, and 9 years computed tomography scans showed slow growth of the nodule to 2.4 cm, corresponding to a volume doubling time of 1494 days. Thoracoscopic biopsy and lobectomy were performed. Pathologic analysis revealed a well-differentiated mucinous BAC (T1N0M0). Pseudocavitation in solitary BAC is rare. A longer period of surveillance may be required to rule out malignancy in this setting. Surgical resection remains the mainstay of therapy.

(Ann Thorac Surg 2008;85:1432–4)

With more widespread use of computed tomography (CT) of the lung, small bronchioloalveolar carcinomas (BACs) are being diagnosed with increasing frequency. Bronchioloalveolar carcinomas are generally thought to have a more indolent course than other subtypes of adenocarcinoma of the lung. While CT appearance varies, the presence of BAC as a solitary cavitary nodule is rare. We report the case of a slow-growing BAC in a young woman that highlights the importance of prolonged surveillance or resection when BAC is included in the differential diagnosis.

A 38-year-old woman with nonpleuritic chest pain and a long-standing right upper lobe cavitary lesion, with a 3 pack-year smoking history, was referred for thoracic surgical evaluation. Nine years previously the patient had been hospitalized because of pneumonia involving the posterior segment of the right upper lobe. Results of tuberculin skin testing were negative. When a chest radiograph at 6-month follow-up showed a persistent mass, a CT scan of the chest was obtained, which revealed a 1.5-cm rounded lesion with central lucency (Fig 1A). Bronchoscopy performed 1 year after initial presentation was nondiagnostic. A chest CT scan obtained 9 years after initial presentation demonstrated the lesion in the right upper lobe measuring 2.4 cm. A fluorodeoxyglucose positron emission tomography scan demonstrated no uptake. Thoracoscopic biopsy followed by lobectomy with lymph node dissection was performed. Pathologic analysis revealed a 2.5-cm well-differentiated mucinous BAC (T1N0M0) (Figs 2, 3). The patient had an uneventful hospital course and was discharged on postoperative day 4.

During nearly a decade, CT scans had been obtained at various institutions, at 6 months and at 1, 3, and 9 years after initial presentation (Figs 1A-D). Review of the scans revealed a largest tumor diameter of 1.5 cm, 1.5 cm, 1.6 cm, and 2.4 cm, respectively, suggesting tumor stability at 1 year. However, calculation of tumor volume from each CT scan ($V = \pi/6 \times ab^2$, where a is the largest diameter and b is the largest diameter perpendicular to a) showed an increase in tumor volume at each interval, with volumes of 1.3 cm^3, 1.4 cm^3, 1.8 cm^3, and 5.6 cm^3, respectively. Tumor

Accepted for publication Oct 1, 2007.

Address correspondence to Dr Shaw, Department of Surgery, Division of Cardiothoracic Surgery, University of Miami Miller School of Medicine, PO Box 016960 (R-114), Miami, FL 33010; e-mail: jason.shaw@mssm.edu.

Published by Elsevier Inc
0003-4975/08/$34.00
doi:10.1016/j.athoracsur.2007.10.031

厚生労働科学研究費補助金
医療機器開発推進研究事業
(活動領域拡張医療機器開発研究事業)

高度医療技術の効率化及び標準化の開発に関する研究

平成20年度　総括・分担研究報告書

研究代表者：廣橋説雄　(2／2冊)

厚生労働科学研究費補助金

医療機器開発推進研究事業

（活動領域拡張医療機器開発研究事業）

高度医療技術の効率化及び
標準化の開発に関する研究

平成２０年度　総括・分担研究報告書

研究代表者　廣橋　説雄

平成２１（２００９）年４月１０日

２／２冊

Tailor-made approach to photodynamic therapy in the treatment of cancer based on Bcl-2 photodamage

JITSUO USUDA[1*], TAKESHI HIRATA[1*], SHUJI ICHINOSE[1], TAICHIROU ISHIZUMI[1], TATSUYA INOUE[1], KEISHI OHTANI[1], SACHIO MAEHARA[1], MASAE YAMADA[1], HIDEMITSU TSUTSUI[1], TETSUYA OKUNAKA[2], HARUBUMI KATO[1] and NORIHIKO IKEDA[1]

[1]Department of Thoracic Surgery, Tokyo Medical University, Tokyo 160-0023; [2]Respiratory Disease Center Sanno Hospital, International University of Health and Welfare, Tokyo 107-0052, Japan

Received April 29, 2008; Accepted June 18, 2008

DOI: 10.3892/ijo_00000054

Abstract. It is very important to elucidate the mechanism of action and identify the molecular determinant of photodynamic medicine, in order to increase the number of clinical applications of photodynamic therapy (PDT) and perform personalized medicine. We have previously reported that PDT using some photosensitizers, such as phthalocyanine 4 (Pc 4) damages the anti-apoptotic protein Bcl-2, and that Bcl-2 is a molecular PDT target using a mitochondrion-targeting photosensitizer. In this study, we examined the molecular targets of Photofrin-PDT and NPe6-PDT, which are approved for early stage lung cancers by the Japanese Ministry of Health Labor and Welfare, by evaluating the photodamage to Bcl-2 using Western blot analysis. Our results showed that Photofrin-PDT damaged Bcl-2, induced morphologically typical apoptosis, and demonstrated equal sensitivity between MCF-7c3 cells (human breast cancer cells expressing stably transfected procaspase-3) and Bcl-2 overexpressing cells, MCF-7c3-GFP-Bcl-2 cells, with a clonogenic assay. However, NPe6-PDT did not damage Bcl-2 and took longer to induce typical apoptosis compared with Photofrin-PDT. MCF-7c3-GFP-Bcl-2 cells were considerably more resistant to the lethal effects of NPe6-PDT than parental MCF-7c3 cells. In conclusion, Photofrin-PDT damages different molecular targets, and our data indicate that the extent of Bcl-2 photodamage can determine the sensitivity of cancer cells to apoptosis and to overall cell killing caused by PDT using Photofrin, but not the lysosomal targeting NPe6. The application of these findings to clinical PDT may depend on the levels of the Bcl-2 proteins in the tumor being treated, and the tailor-made medicine based on the Bcl-2 photodamage may overcome any resistance afforded by elevated amounts of Bcl-2.

Correspondence to: Dr J. Usuda, Department of Thoracic Surgery, Tokyo Medical University, 6-7-1 Nishishinjuku, Shinjuku-ku, Tokyo 160-0023, Japan
E-mail: jusuda@tokyo-med.ac.jp

*Contributed equally

Key words: photodynamic therapy, photofrin, NPe6, Bcl-2 photodamage, personalized medicine, tailor-made approach

Introduction

Photodynamic therapy (PDT), used as a treatment modality for many cancers, uses a tumor-specific photosensitizer and laser irradiation to induce the production of reactive oxygen species in cancer cells (1,2). Since the report of the first modern clinical trial of PDT by Dougherty *et al* in 1978 (3), PDT using the photosensitizer, Photofrin, has been applied for the treatment of many cancers, and is approved by the United States Food and Drug Administration (FDA) for the treatment of early stage lung cancer as well as advanced esophageal and lung cancers (1,2,4-6). In Japan, PDT is recommended as a treatment option for centrally located early-stage lung cancer in the therapeutic guidelines for lung cancer established by the Japanese Ministry of Health, Labor and Welfare using the principles of evidence-based medicine (7,8). Recently, a second generation photosensitizer, mono-L-asparyl chlorine e6 (talaporfin sodium, Laserphyrin, NPe6), which has a major absorption band at 664 nm, was approved for use in the diagnosis/treatment of centrally located early-stage lung cancer by the Japanese government (9,10). In order to enhance the efficacy of PDT and extend its applications, it is very important to choose photosensitizers according to the pathological characteristics of malignant tumors, which have elevated amounts of Bcl-2.

We reported that PDT using phthalocyanine (Pc) 4 and red light damaged the antiapoptotic protein Bcl-2 (11,12). We have reported on the construction of a series of Bcl-2 mutants and the examination of the association between their subcellular organelles and their sensitivity to photodestruction by Pc 4-PDT, which mainly damaged the mitochondria and induced apoptosis. Pc 4-PDT damaged Bcl-2 photochemically, but the photodamaged Bcl-2 is neither phosphorylated nor converted to a proapoptotic molecule. Photodamage destroys the ability of Bcl-2 to prevent apoptosis, but when high levels of overexpressed Bcl-2 or functional mutants are present, high doses are required to produce sufficient photodamage to inactivate the large amounts of Bcl-2 (12). The extent of Bcl-2 photodamage determined the sensitivity of cancer cells to apoptosis and overall cell killing caused PDT.

It was reported that Photofrin localizes in the mitochondria and endoplasmic reticulum (ER), and NPe6 localized lysosomes (13). Reiners *et al* (14) reported that lysosomes photodamaged by NPe6-PDT trigger the mitochondrial apoptotic pathway by releasing the proteases cathepsin B, L and D, which are lysosomal cytokine proteinases and act as the main executors of caspase-independent and/or caspase-dependent cell death.

We hypothesized that differences existed in the mechanism of action behind the anti-cancer effects between Photofrin-PDT and NPe6-PDT based on different subcellular localizations. In this study, in order to elucidate the possibility of tailor-made medicine for cancer treatment based on Bcl-2 expression using Photofrin-PDT or NPe6-PDT, we studied transient and stable transfectants that overexpress either the wild-type Bcl-2 or a Bcl-2 mutant, and we investigated the apoptotic response via mitochondrial and/or lysosomal damage.

Materials and methods

Cell culture. Human breast cancer MCF-7 cells transfected with human procaspase-3 cDNA (MCF-7c3 cells) were cultured in RPMI-1640 medium containing 10% fetal bovine serum (11,12). MCF-7c3 cells were transfected with GFP, GFP-Bcl-2, GFP-Bcl-2Δ (33-54), GFP-Bcl-2Δ (153-179) and GFP-Bcl-2Δ (210-239) plasmids and we isolated all stable transfected cells, using a limiting dilution method. These cells were cultured in RPMI-1640 medium. The cultures were maintained in a humidified atmosphere at 37˚C with 5% CO_2 (11,12).

Photosensitizers. Photofrin (Wyeth Japan K.K., Tokyo, Japan), a hydrophobic hematoporphyrin derivative, remains a complex mixture with inherent variability, and its tumor affinity is strong. It is activated by a highly transmissive red light wavelength of 630 nm, and produces a photochemical reaction (4-6). NPe6 (Meiji Seika, Tokyo, Japan) is a second generation water-soluble photosensitizer which has a molecular weight of 799.69 and a chlorine annulus, and has its highest absorption peak at wavelengths of 407 nm and a second peak at 664 nm (9,10). NPe6 is superior in tumor affinity to Photofrin, and allows excitation with the longer visible red wavelength of 664 nm, which gives a deeper and better penetration to living tissue.

Laser unit. An excimer dye laser (Hamamatsu Photonics K.K., Hamamatsu, Japan) emitting pulse-wave laser light at a wavelength of 630 nm was used as the light source for the excitation of Photofrin (4-6). A diode laser (Matsushita Electric Industrial Co., Osaka, Japan) emitting continuous-wave laser light at a wavelength of 664 nm was used as the light source for excitation of NPe6 (9,10).

Fluorescence microscopy. Fluorescence images were acquired using the handstand-type fluorescence microscope (Diaphot TMD-EF2, Nikon, Tokyo, Japan) with the transfer device of a high-speed excitation light wavelength and the fluorescence imaging system with the high-speed cooling CCD camera (Panasonic Model BD900: Matsushita Electric Industrial Co.), on the excitation Xenon light of 405 nm, the detection wavelength >600 nm for NPe6 and the detection wavelength of 630 nm for Photofrin (11,12,15). For the live fluorescence imaging of MCF-7c3-GFP cells, the cells were plated on 35-mm glass-bottomed dishes (MatTek Corp., Ashland, MA) and incubated with 100 nM LysoTracker Blue (Molecular Probes, Eugene, OR, USA) or 100 nM MitoTracker Green (Molecular Probes) for 45 min at 37˚C. Images of the LysoTracker Blue fluorescence were collected using a 543-nm excitation light from a helium-neon (He-Ne) laser and a 560 nm long-pass filter. Images of the MytoTracker Green fluorescence were collected using a 490-nm excitation light from a He-Ne laser and a 516 nm long-pass filter.

DNA gene transfection. We used lipofectamine (Invitrogen, Carlsbad, CA, USA) and performed a gene transfection of 2 μg of the plasmid genes, which were pcDNA/His/Max-Bcl-2, pcDNA/His/Max-Bcl-2Δ (33-54), pcDNA/His/Max-Bcl-2Δ (153-179), and pcDNA/His/Max-Bcl-2Δ (210-239), in the MCF-7c3 cell line (11,12).

Western blot analysis. Cells were harvested by centrifugation and washed twice with ice-cold PBS. The cell pellets were incubated in a lysis buffer (50 mM Tris-HCl, pH 7.5, 120 mM NaCl, 1% Triton X-100, 0.2% sodium dodecyl sulfate (SDS), 0.5% deoxycholate, 10 μg/ml leupeptin, 10 μg/ml aprotinin, 1 mM phenylmethylsulfonyl fluoride and 100 mM NaF) on ice for 30 min and then sonicated (11,12,15). The protein content of the whole-cell lysates was measured using the BCA protein assay reagent (Pierce, Rockford, IL). Aliquots (20 μg) of the whole-cell lysates were separated by SDS-polyacrylamide gel electrophoresis (PAGE) and transferred to polyvinylidene difluoride membranes. The membranes were incubated with one of the following antibodies at appropriate concentrations for 1 h: mouse monoclonal anti-Xpress (Invitrogen, Carlsbad, CA, USA), mouse monoclonal anti-actin (Santa Cruz Biotechnology, Inc., Santa Cruz, CA, USA) and hamster monoclonal anti-human Bcl-2 (Pharmingen, San Diego, CA, USA) (11,12). After rinsing with PBS containing 0.1% (vol/vol) Triton X-100, the membranes were incubated with anti-mouse or anti-hamster immunoglobulin G conjugated to horseradish peroxidase for 1 h at room temperature. The membranes were washed and developed with Western blotting-enhanced chemiluminescence detection reagents (Amersham Pharmacia Biotech, Piscataway, NJ, USA). Independent experiments were repeated at least three times.

Nuclear-staining assay for apoptosis. For PDT, cells were treated with 0.63 μg/ml Photofrin or with 1.75 μg/ml NPe6 for 3 h and then irradiated with red light (3 J/cm^2, 150 mW). Zero, 6, or 24 h after PDT, cells were collected and fixed in 1% formaldehyde. After being fixed, the cells were stained with Hoechst 33342 (Molecular Probes). At least 200 cells were counted from each sample, and the yield of apoptotic cells was expressed as a percentage of the total population. Independent experiments were repeated at least three times (11,12).

Clonogenic MCF-7c3-GFP or MCF-7c3-GFP-Bcl-2 cell survival. Exponentially growing cultures of MCF-7c3-GFP or MCF-7c3-GFP-Bcl-2 cells were treated with 0, 0.31, 0.63,

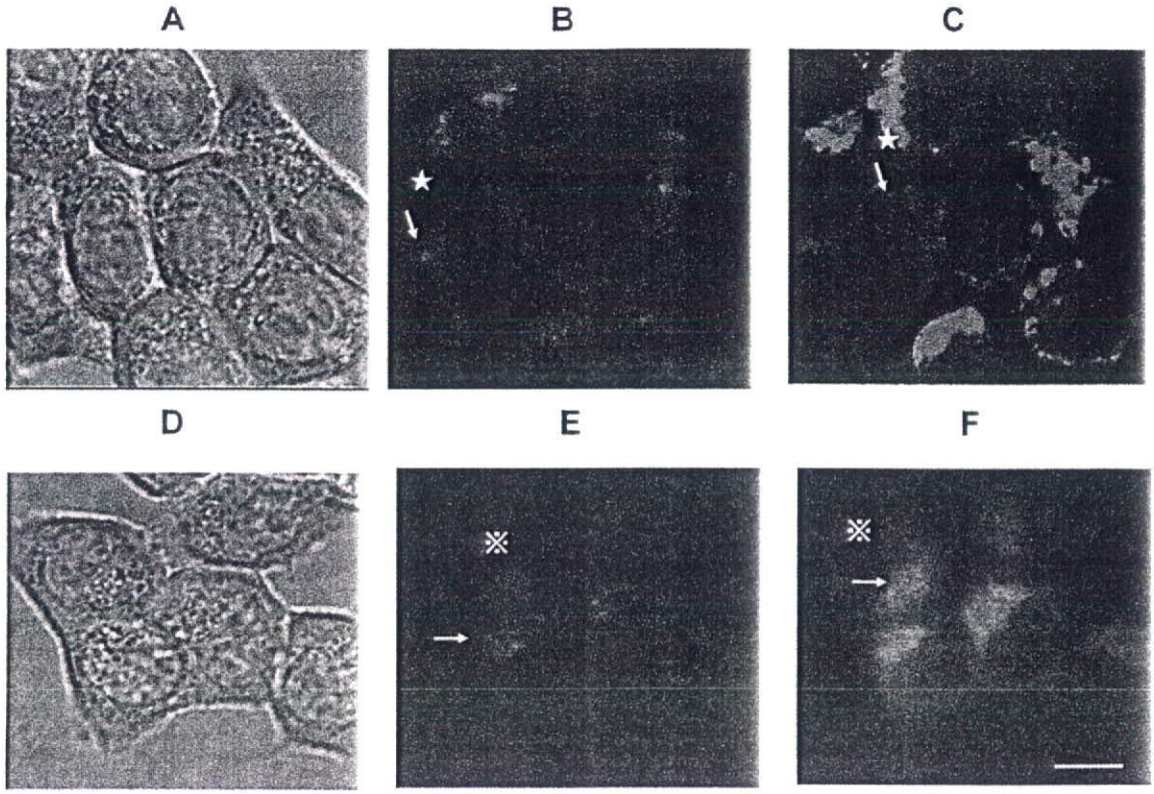

Figure 1. Localization of Photofrin and NPe6 in MCF-7c3 cells. MCF-7c3 cells were loaded with 0.63 μg/ml Photofrin for 3 h (A, B and C) and 100 nm MitoTracker Green. The images in A and D are conventional white light microscopical findings. The images of Photofrin displayed diffuse and punctate patterns (B). The pattern types did not completely co-localize when cells were loaded with MitoTracker Green (C). The sign (⋆) showed the localization of the mitochondria. MCF-7c3 cells were loaded with 1.75 μg/ml NPe6 for 3 h (D, E and F) and 100 nm LysoTracker Blue. The images of NPe6 displayed some punctate and some diffuse patterns (E). The pattern types did not completely co-localize when cells were loaded with LysoTracker Blue (F). The sign ※ shows the localization of lysosome. Scale bar, 5 μm.

1.25, 1.75 and 2.0 μg/ml Photofrin or NPe6 for 3 h and then irradiated with laser light (3 J/cm^2). Immediately after PDT, cells were trypsinized, collected, diluted and plated at appropriate concentrations. Aliquots of the cells were seeded into 60-mm dishes in amounts sufficient to yield 50-150 colonies. After incubation for 14 days, the cells were stained with 0.1% crystal violet in 20% ethanol, and colonies containing >50 cells were counted. The plating efficiency of untreated cells was 30-40%. Each datum is the mean ± standard deviation of results from three independent experiments (11,12,16).

Results

Photofrin mainly localizes to the mitochondria and NPe6 localizes to the lysosomes of MCF-7c3 cells. In cancer cells, PDT produces singlet oxygen and other reactive oxygen species in the membranes and causes photooxidative damage to proteins and lipids that reside within a few nm of the photosensitizer binding sites. To elucidate the mechanism of action of PDT, it has been reported that localization of the photosensitizer is important. We first examined the localization of Photofrin and NPe6 in MCF-7c3 cells using fluorescence microscopy (Fig. 1A-F). In order to assess whether Photofrin binds to the mitochondria, MCF-7c3 cells were co-loaded with MitoTracker Green, a mitochondria-specific dye. The images of Photofrin displayed diffuse and punctate patterns (B). Photofrin fluorescence showed a slight tendency to co-localize with MitoTracker green fluorescence, but without total co-localization (C). These results suggest that in MCF-7c3 cells Photofrin localizes not only to the mitochondria but also to the endoplasmic reticulum (ER), Golgi complexes and possibly other intracellular organelles. However, it does not localize to the plasma membrane or the nucleus.

In contrast, the images of NPe6 displayed some punctate and some diffuse patterns (E), and mainly co-localize with LysoTracker Blue (F). These results suggest that NPe6 induces the destruction of lysosomes as previously reported (13,14,17).

Photofrin-PDT photodamaged the anti-apoptotic protein Bcl-2. We have reported that PDT using the photosensitizer Pc 4 and red light damages the anti-apoptotic protein Bcl-2 (11,12,18,19). We used pcDNA4/HisMax plasmid, which encodes the Xpress™ epitope at the N-terminal region of the multiple cloning sites (11,12). We transiently transfected pcDNA4/HisMax-full-length human Bcl-2 (239 amino acids) into MCF-7c3 cells. Twenty-four hours after the transfection, we performed Photofrin-PDT (3 J/cm^2). The dose (1 μg/ml) produced a ~93±3% killing of MCF-7c3 cells, as determined by clonogenic assay (Fig. 4A). The extent of the photodamage was assessed with Western blot analysis (Fig. 2A). The over-expressed wild-type Bcl-2 was immediately photodamaged by Photofrin-PDT at doses of 0.16, 0.31, 0.63 μg/ml and

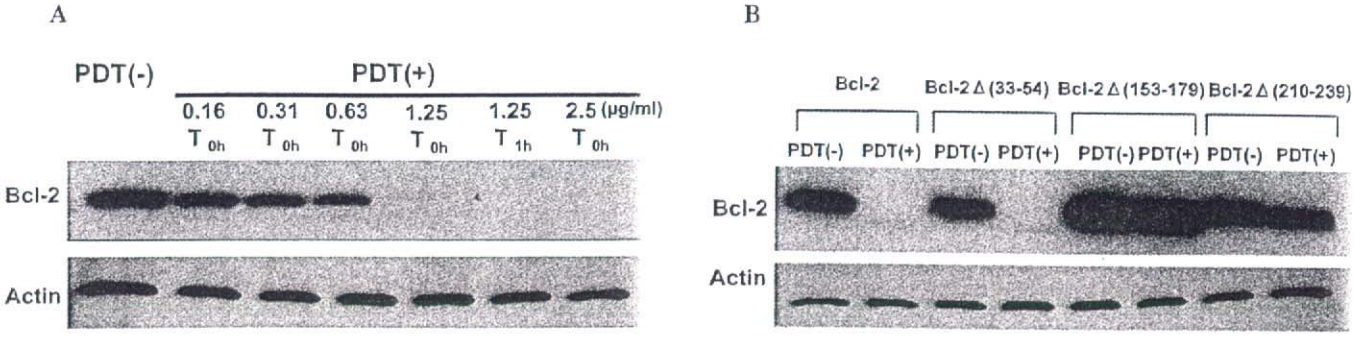

Figure 2. (A) Photodamage to Bcl-2 in MCF-7c3 cells by Photofrin-PDT. MCF-7c3 cells were transiently transfected with a PcDNA/HisMax expression vector containing wild-type Bcl-2, pcDNA/His/Max-Bcl-2. Twenty-four hours after transfection, the cells were treated with 0.16, 0.31, 0.63, 1.25 and 2.0 μg/ml Photofrin for 3 h and then irradiated with laser (630 nm, 3 J/cm²). Immediately (T_{0h}), or 1 h (T_{1h}) after PDT, cells were collected, washed and lysed. An aliquot (20 μg) of the whole cell lysate was separated by SDS-PAGE. The Bcl-2 level was examined on Western blots using a mouse monoclonal anti-Xpress antibody. The membrane was re-probed with anti-actin as a control. (B) Photodamage to mutant Bcl-2 in MCF-7c3 cells caused by Photofrin-PDT. MCF-7c3 cells were transiently transfected with pcDNA/His/Max-Bcl-2Δ (33-54) or pcDNA/His/Max-Bcl-2Δ (153-179) or pcDNA/His/Max-Bcl-2Δ (210-239). Twenty-four hours after transfection, the cells were treated with 0.63 μg/ml Photofrin for 3 h and then irradiated with laser (630 nm, 3 J/cm²) producing a 90% killing of MCF-7c3 cells. Immediately after PDT, cells were collected, washed and lysed. An aliquot (20 μg) of the whole cell lysate was separated by SDS-PAGE. The mutant Bcl-2 level was examined on Western blots using a mouse monoclonal anti-Xpress antibody. The membrane was reprobed with anti-actin as the control.

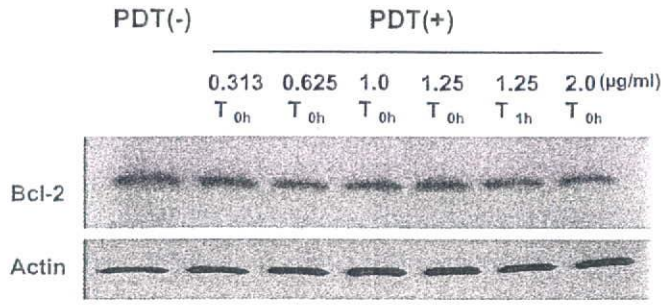

Figure 3. Photodamage to Bcl-2 in MCF-7c3 cells caused by laserphyrin-PDT. MCF-7c3 cells were transiently transfected with a PcDNA/HisMax expression vector containing wild-type Bcl-2, pcDNA/His/Max-Bcl-2. Twenty-four hours after transfection, the cells were treated with 0.63, 1.0, 1.25, 1.75 and 2.5 μg/ml laserphyrin for 3 h and then irradiated with laser (630 nm, 3 J/cm²). Immediately (T_{0h}), or 1 h (T_{1h}) after PDT, cells were collected, washed and lysed. An aliquot (20 μg) of the whole cell lysate was separated by SDS-PAGE. The Bcl-2 level was examined on Western blots using a mouse monoclonal anti-Xpress antibody. The membrane was reprobed with anti-actin as the control. Scale bar, 10 μm.

almost disappeared at doses of 1.25, 2.5 μg/ml. One hour after PDT at the 1.25 μg/ml dose, despite using Pc 4-PDT, the levels of the wild-type Bcl-2 protein had not been restored to their previous level (Fig. 2A) as we have previously reported. These results indicate that Photofrin-PDT damages Bcl-2 as Pc 4-PDT (11).

In a similar manner to the overexpressed wild-type Bcl-2, a mutant with deletions in the N-terminal half of Bcl-2, Bcl-2Δ (33-54), was immediately photodamaged by Photofrin-PDT as Pc 4-PDT (Fig. 2B). These results indicate that there is no essential target site of Photofrin-PDT in the N-terminal half of Bcl-2, and Asp-34, a known caspase cleavage site (20,21), is not required for photodamage to Bcl-2 by Photofrin-PDT as previously reported (11,12). The region between the BH1 and BH2 domains, which contains the two core hydrophobic α-helices (α5 and α6), is required for membrane insertion and channel formation. Bcl-2 (Δ153-179), which deletes the two core regions, was not photodamaged by Photofrin-PDT (Fig. 2B). Moreover, Bcl-2 (Δ210-239) which is lacking the C-terminal transmembrane domain, was not photodamaged by Photofrin-PDT either (Fig. 2B). These results indicate that the site of Bcl-2 localization is accessible for photodamage and that Photofrin must reside within a few nm of the Bcl-2 binding sites in the mitochondrial, ER and perinuclear membranes as reported in our previous data using Pc 4-PDT (11,12,18,19).

NPe6-PDT did not photodamage the anti-apoptotic protein Bcl-2. We did not observe any Bcl-2 photodamage by NPe6-PDT (Fig. 3). These results suggest that NPe6 localizes mainly in the lysosomes and resides far from the Bcl-2 binding sites, and that NPe6-PDT did not directly damage the mitochondrial membrane. The mechanisms of action of NPe6-PDT may differ from those of photofrin-PDT or Pc 4-PDT.

Bcl-2-overexpressing cells were resistant to loss of clonogenicity after NPe6-PDT. We previously isolated and characterized clones of MCF-7c3 cells stably overexpressing high levels of GFP-Bcl-2 (12). MCF-7c3-GFP-Bcl-2 cells were 50-fold the levels of Bcl-2 of the parental MCF-7c3 cells (12). We evaluated the sensitivity of MCF-7c3-GFP cells to Photofrin-PDT or NPe6-PDT with a clonogenic assay. The survival curves (Fig. 4 upper panel) indicate that MCF-7c3 cells overexpressing GFP-Bcl-2 were not resistant compared to the parental MCF-7c3 cells after Photofrin-PDT. At the 10% survival level, the presence of Bcl-2 provided a dose-modifying factor of ~1.1. However, Fig. 4 lower panel show that MCF-7c3 cells overexpressing GFP-Bcl-2 were considerably more resistant to the lethal effects of NPe6-PDT than were the parental MCF-7c3 cells. These results suggest that Bcl-2 exerts a marked regulatory effect on the cell survival of NPe6-PDT.

Photofrin-PDT revealed many morphologically typical apoptotic signs. In order to examine whether stable expression of the Bcl-2 protein can protect against apoptosis induced by

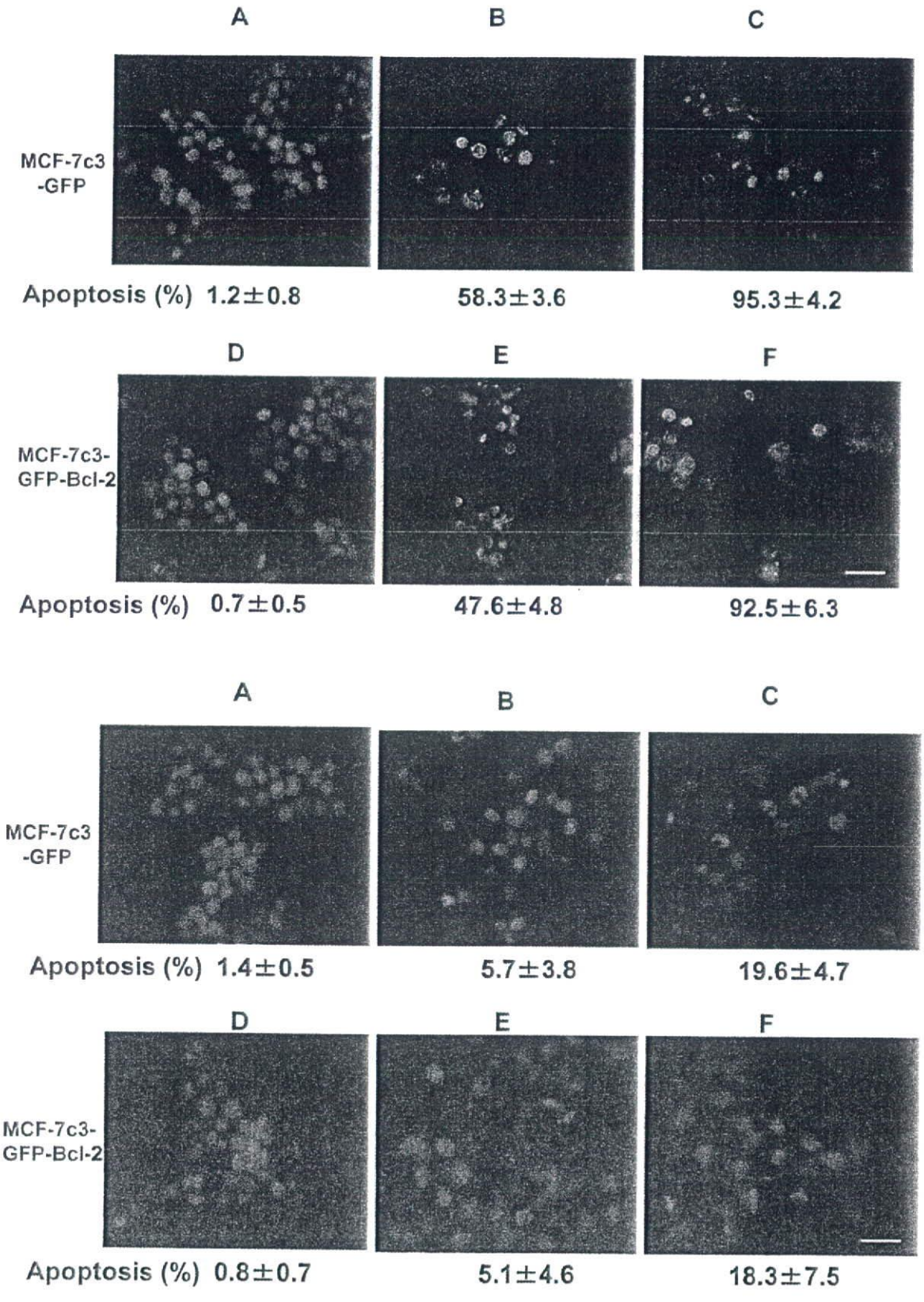

Figure 4. Upper panel. Photofrin-PDT induced morphologically typical apoptosis. MCF-7c3-GFP (A, B and C) and MCF-7c3-GFP-Bcl-2 cells (D, E and F) were treated with 0.63 μg/ml Photofrin for 3 h and then irradiated with laser light (630 nm, 3 J/cm^2), producing a 90% killing of MCF-7c3 cells, as determined with clonogenic assay. Cells were collected and fixed either before PDT (A and D), or 6 h (B and E) or 24 h (C and F) after PDT. After being fixed, the cells were stained with Hoechst 33342. At least 200 cells were counted from each sample and the yield of apoptotic cells was expressed as a percentage of the total population. Scale bar, 10 μm. Lower panel. NPe6-PDT did not induce morphologically typical apoptosis. MCF-7c3-GFP (A, B and C) and MCF-7c3-GFP-Bcl-2 cells (D, E and F) were treated with 1.75 μg/ml NPe6 for 3 h and then irradiated with laser light (664 nm, 3 J/cm^2), producing a 90% killing of MCF-7c3 cells, as determined by clonogenic assay. Cells were collected and fixed either before PDT (A and D), or 6 h (B and E) or 24 h (C and F) after PDT. After being fixed, the cells were stained with Hoechst 33342. At least 200 cells were counted from each sample and the yield of apoptotic cells was expressed as a percentage of the total population.

A

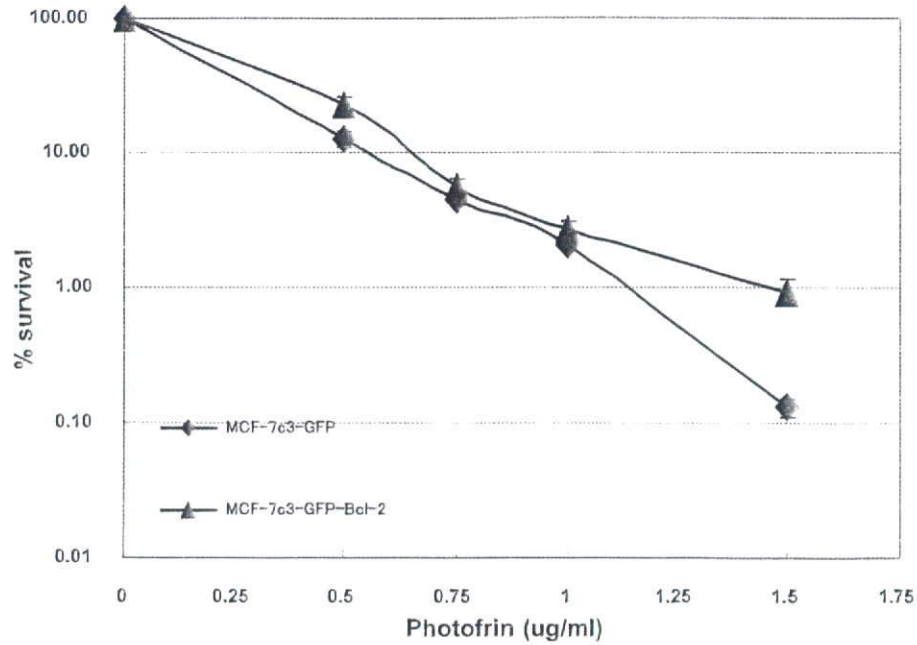

B

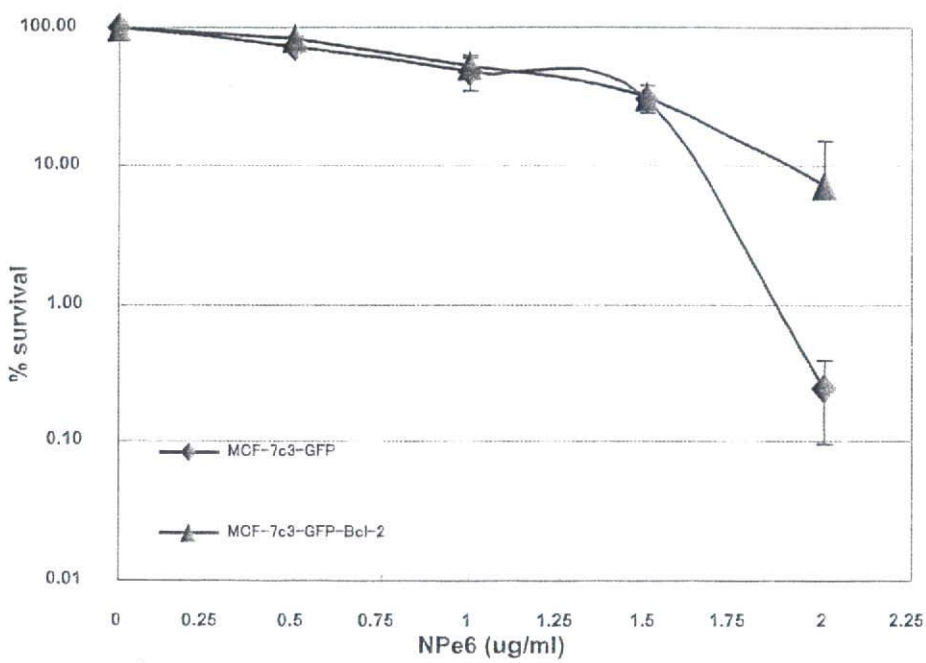

Figure 5. (A) Loss of clonogenicity of MCF-7c3-GFP and MCF-7c3-GFP-Bcl-2 cells as a result of Photofrin-PDT. Exponentially growing cultures of each cell line were treated with 0.16, 0.31, 0.63, 1.25 and 2.5 μg/ml Photofrin for 3 h and then irradiated with laser (630 nm, 3 J/cm^2). Immediately after PDT, cells were trypsinized, collected, diluted and plated at appropriate concentrations. We compared PDT-treated and -untreated cells of the same cell line with regard to plating efficiency. Each datum is the mean ± standard deviation of the result from three independent experiments. (B) Loss of clonogenicity of MCF-7c3-GFP and MCF-7c3-GFP-Bcl-2 cells as a result of NPe6-PDT. Exponentially growing cultures of each cell line were treated with 0.31, 0.63, 1.25, 1.75 and 2.5 μg/ml NPe6, for 3 h and then irradiated with laser (664 nm, 3 J/cm^2). Immediately after PDT, cells were trypsinized, collected, diluted and plated at appropriate concentrations. We compared PDT-treated and -untreated cells of the same cell line with regard to plating efficiency. Each datum is the mean ± standard deviation of the result from three independent experiments.

Photofrin-PDT, we estimated apoptosis by monitoring the nuclear morphology after staining with Hoechst 33342. We examined for the presence of apoptosis caused by Photofrin-PDT. We used the MCF-7c3-GFP cell line that stably produced only the pEGFP vector (Clontech, Palo Alto, CA, USA) to the MCF-7c3 cell line. The MCF-7c3-GFP-Bcl-2 cell line over-expressed the Bcl-2 protein, but was resistant to apoptosis by staurosporine (STS), a protein kinase C (PKC) inhibitor (11,12). We performed PDT for the MCF-7c3-GFP-Bcl-2 cell line which stably overexpressed the Bcl-2 protein under the same conditions as for the MCF-7c-GFP cell line. When we attempted to damage Bcl-2 in MCF-7c3 cells under LD_{90} dose condition with Photofrin-PDT, cells progressed to morphologically typical apoptosis in a very short period, with

more than ~50% of cells being in apoptosis within 6 h and >90% of cells within 24 h (Fig. 5A). Twenty-four hours after Photofrin-PDT, apoptotic cells accounted for 95.3±4.2% in the MCF-7c3 and 92.5±6.3% in the MCF-7c3-GFP-Bcl-2 cell lines, but there was no statistically significant difference between the cell lines (P=0.4119).

NPe6-PDT achieved mild morphologically typical apoptosis. We performed PDT under the same LD_{90} dose conditions to assess apoptosis caused by NPe6-PDT and performed Hoechst staining afterwards (Fig. 5B). MCF-7c3-GFP and MCF-7c3-GFP-Bcl-2 cell line images showed a few percentage points of morphologically typical apoptosis 6 h after PDT, with 20% of typical apoptosis 24 h after PDT. The percentages of apoptotic cells after 24 h of Photofrin-PDT and NPe6-PDT were 95.3±4.2 and 19.6±4.7%, respectively, with a significant difference seen in the MCF-7c3-GFP cell line (P=0.008). For the MCF-7c3-GFP-Bcl-2 cell line, the apoptotic percent-ages were 92.5±6.3 and 18.3±7.5%, respectively, again with a significant difference (P=0.009). These results suggest the antitumor effect of NPe6-PDT was quite different from that of Photofrin-PDT.

Discussion

It has been reported that PDT induces direct tumor cell death as well as indirect effects on the tumor microenvironment (2-5). PDT rapidly induces apoptosis, inflammatory reactions, tumor-specific and/or non-specific immune reactions and damage of the microvasculature of the tumor bed (4-6,22-24). Apoptosis has also been reported as not a necessary component of post-PDT cell death, and PDT has been reported as cytotoxic to sensitized cells that have defects in their apoptotic program (19,25-27). Moreover, autophagy, which was originally described as a survival response to nutrient deprivation, occurs during PDT protocols involving photosensitizers that localize to the ER. The form of cell death induced by autophagy is distinct from apoptosis, and the relationship between autophagy and apoptosis is important to PDT-mediated tumor cell death.

In this study, we have shown that Photofrin-PDT damaged the Bcl-2 protein and induced apoptosis in Bcl-2 or a certain Bcl-2 mutant, Bcl-2Δ (33-54) overexpressing cells. Moreover, we found that membrane anchorage regions were needed to form the target of Photofrin photosensitization, and that photodamage required the region between the Bcl-2 homology 1 (BH1) and BH2 domains, which contains two hydrophobic α-helices (α5 and α6). These data are similar to our previous reports on the use of Pc 4 (11,12). However, Bcl-2 overexpressing cells were neither resistant to the induction nor loss of clonogenicity on exposure to Photofrin-PDT. The role of Bcl-2 in the apoptotic response caused by PDT remains controversial. We have previously reported that the extent of Bcl-2 photodamage may determine the sensitivity of cancer cells to apoptosis and overall cell killing caused by Pc 4-PDT (11). As shown in Fig. 2B, the Bcl-2 protein was completely damaged and lost following Photofrin-PDT in MCF-7c3-GFP-Bcl-2 cells, which were 50 times the level of Bcl-2 as the parental MCF-7c3 cells (11). Kessel *et al* reported that loss of the Bcl-2 protein or function can also initiate the development of autophagy (26,27). Our data suggest that Photofrin-PDT can induce cell killing via apoptosis and/or autophagy independently of the Bcl-2 expression.

The overexpressed wild-type Bcl-2 was not immediately photodamaged by NPe6-PDT (Fig. 3). Moreover, NPe6-PDT did not rapidly induce morphologically typical apoptosis in MCF-7c3 cells. Under the LD_{90} dosage conditions, 5-9 and 20-25% of cells were apoptotic within 6 and 12 h, respectively, and NPe6-PDT took longer to induce apoptosis compared with Photofrin-PDT. Reiners *et al* reported that lysosomes photodamaged by NPe6-PDT trigger the mitochondrial apoptotic pathway by releasing the proteases, cathepsin B, L and D, which are lysosomal cytokine proteinases (14). Our data suggest that lysosomal damage triggers the apoptotic signal after NPe6-PDT and the apoptotic pathway caused by NPe6-PDT differs from Photofrin-PDT. NPe6-PDT did not cause photodamage to Bcl-2. Therefore, MCF-7c3-GF-Bcl-2 cells were resistant to the lethal effects as demonstrated with the clonogenic assay (Fig. 4). According to Xue *et al*, PDT-induced Bcl-2 photodamage disrupted the binding of Bcl-2 to Beclin 1, resulting in the elimination of an effect of Bcl-2 on PDT-induced autophagy (19,28,29). Our data suggest that for NPe6-PDT, Bcl-2 overexpression protects against apoptosis as well as autophagy, and exerts marked regulatory effects on cell survival.

Many advanced cancers have elevated amounts of the Bcl-2 protein (30,31) and we hypothesize that Bcl-2 photo-damage by Photofrin-PDT eliminates their normal protection against cell death, but not by NPe6-PDT. In conclusion, the application of these findings to clinical PDT may depend on the levels of the Bcl-2 proteins in the tumor being treated, and the tailor-made medicine based on the Bcl-2 photodamage may overcome any resistance afforded by elevated amounts of Bcl-2.

Acknowledgements

This study was supported in part by a Grant-in-Aid for Japan Society for the Promotion of Science (JSPS) Fujita Memorial Fund for Medical Research (to J.U.)

References

1. Dougherty TJ, Gomer CJ, Barbara WH, *et al*: Photodynamic therapy. J Natl Cancer Inst 90: 889-905, 1998.
2. Henderson BW and Dougherty TJ: How does photodynamic therapy work? Photochem Photobiol 55: 145-157, 1992.
3. Dougherty TJ: Photoradiation therapy for the treatment of malignant tumors. Cancer Res 36: 2628-2635, 1978.
4. Oleinick NL, Morris RL and Belichenko I: The role of apoptosis in response to photodynamic therapy: what, where, why, and how. Photochem Photobiol Sci 1: 1-21, 2001.
5. Gomer CJ, Ferrario A, Luna M, *et al*: Photodynamic therapy: Combined modality approaches targeting the tumor micro-environment. Lasers Surg Med 38: 516-521, 2006.
6. Dougherty TJ: An update on photodynamic therapy applications. J Clin Laser Med Surg 20: 3-7, 2002.
7. Usuda J, Kato H, Okunaka T, *et al*: Photodynamic therapy for lung cancers. J Thorac Oncol 1: 489-493, 2006.
8. Kato H, Usuda J, Okunaka T, *et al*: Basic and clinical research on photodynamic therapy at Tokyo Medical University Hospital. Lasers Surg Med 38: 371-375, 2006.
9. Kato H, Furukawa K, Sato M, *et al*: Phase II clinical study of photodynamic therapy using mono-L-aspartyl chlorine e6 and diode laser for early superficial squamous cell carcinoma of the lung. Lung Cancer 42: 103-111, 2003.

10. Usuda J, Tsutsui H, Honda H, *et al*: Photodynamic therapy for lung cancers based on novel photodynamic diagnosis using talaporfin sodium (NPe6) and autofluorescence bronchoscopy. Lung Cancer 58: 317-323, 2007.
11. Usuda J, Chiu SM, Murphy ES, *et al*: Domain-dependent photodamage to Bcl-2: A membrane anchorage region is needed to form the target of phthalocyanine photosensitization. J Biol Chem 278: 2021-2029, 2003.
12. Usuda J, Azizuddin K, Chiu SM, *et al*: Association between the photodynamic loss of Bcl-2 and the sensitivity to apoptosis caused by phthalocyanine photodynamic therapy. Photochem Photobiol 78: 1-8, 2003.
13. Kessel D, Luo Y, Mathieu P, *et al*: Determinants of the apoptotic response to lysosomal photodamage. Photochem Photobiol 71: 196-200, 2000.
14. Reiners JJ, Caruso JA, Mathieu P, *et al*: Release of cytochrome c and activation of procaspase-9 following lysosomal photodamage involves Bid cleavage. Cell Death Differ 9: 934-944, 2002.
15. Usuda J, Okunaka T, Furukawa K, *et al*: Increased cytotoxic effects of photodynamic therapy in IL-6 gene transfected cells via enhanced apoptosis. Int J Cancer 93: 475-480, 2001.
16. Okunaka T, Usuda J, Ichinose S, *et al*: A possible relationship between the anti-cancer potency of photodynamic therapy using the novel photosensitizer ATX-s10-Na(II) and expression of the vascular endothelial growth factor *in vivo*. Oncol Rep 18: 679-683, 2007.
17. Ichinose S, Usuda J, Hirata T, *et al*: Lysosomal cathepsin initiates apoptosis, which is regulated by photodamage to Bcl-2 at mitochondria in photodynamic therapy using a novel photosensitizer, ATX-s10(Na). Int J Oncol 29: 349-355, 2006.
18. Xue LY, Chiu SM and Oleinick NL: Photochemical destruction of the Bcl-2 oncoprotein during photodynamic therapy with the phthalocyanine photosensitizer Pc 4. Oncogene 20: 3420-3427, 2001.
19. Xue LY, Chiu SM, Azizuddin K, *et al*: The depth of human cancer cells following photodynamic therapy: Apoptosis competence is necessary for Bcl-2 protection but not for induction of autophagy. Photochem Photobiol 83: 1016-1023, 2007.
20. Cheng EHY, Kirsch DG, Clen RJ, *et al*: Conversion of Bcl-2 to a Bax-like death effector by caspases. Science 278: 1966-1968, 1997.
21. Kirsch DG, Doseff A, Chau BN, *et al*: Caspase-3-dependent cleavage of Bcl-2 promotes release of cytochrome c. J Biol Chem 274: 21155-21161, 1999.
22. Ferrario A, von Tiehil KF, Rucker N, Schwartz MA, Gill PS and Gomer CJ: Antiangiogenic treatment enhances photodynamic therapy responsiveness in a mouse mammary carcinoma. Cancer Res 60: 4066-4069, 2000.
23. Korbelik M: PDT-associated host response and its role in the therapy outcome. Lasers Surg Med 38: 500-508, 2006.
24. Gollnick SO, Owczarczak B and Maier P: Photodynamic therapy and anti-tumor immunity. Lasers Surg Med 38: 509-515, 2006.
25. Amaravadi RK and Thompson CB: The roles of therapy-induced autophagy and necrosis in cancer treatment. Clin Cancer Res 13: 7271-7279, 2007.
26. Kessel D, Vicente HG and Reiners JJ: Initiation of apoptosis and autophagy by photodynamic therapy. Lasers Surg Med 38: 482-488, 2006.
27. Kessel D and Reiners J: Apoptosis and autophagy after mitochondrial or endoplasmic reticulum photodamage. Photochem Photobiol 83: 1024-1028, 2007.
28. Saeki K, You A, Okuma E, *et al*: Bcl-2 down-regulation causes autophagy in a caspase-independent manner in human leukemia HL-60 cells. Cell Death Differ 7: 1263-1269, 2000.
29. Pattingre S, Tassa A, Qu X, *et al*: Bcl-2 antiapoptotic proteins inhibit beclin 1-dependent autophagy. Cell 122: 927-939, 2005.
30. Kawaguchi T, Yamamoto S, Naka N, *et al*: Immunohistochemical analysis of bcl-2 protein in early squamous cell carcinoma of the bronchus treated with photodynamic therapy. Br J Cancer 82: 418-423, 2000.
31. Ohnuma Y, Aoe M, Andou A, *et al*: Telomerase activity and Bcl-2 expression in non-small cell lung cancer. Clin Cancer Res 6: 2980-2987, 2000.

In vivo Optical Coherence Tomography Imaging of Preinvasive Bronchial Lesions

Stephen Lam,[1] Beau Standish,[2] Corisande Baldwin,[1] Annette McWilliams,[1] Jean leRiche,[1] Adi Gazdar,[3] Alex I. Vitkin,[2] Victor Yang,[2] Norihiko Ikeda,[4] and Calum MacAulay[1]

Abstract

Purpose: Optical coherence tomography (OCT) is an optical imaging method that can visualize cellular and extracellular structures at and below tissue surface. The objective of the study was to determine if OCT could characterize preneoplastic changes in the bronchial epithelium identified by autofluorescence bronchoscopy.

Experimental Design: A 1.5-mm fiberoptic probe was inserted via a bronchoscope into the airways of 138 volunteer heavy smokers participating in a chemoprevention trial and 10 patients with lung cancer to evaluate areas that were found to be normal or abnormal on autofluorescence bronchoscopy. Radial scanning of the airways was done to generate OCT images in real time. Following OCT imaging, the same sites were biopsied for pathologic correlation.

Results: A total of 281 OCT images and the corresponding bronchial biopsies were obtained. The histopathology of these areas includes 145 normal/hyperplasia, 61 metaplasia, 39 mild dysplasia, 10 moderate dysplasia, 6 severe dysplasia, 7 carcinoma *in situ*, and 13 invasive carcinomas. Quantitative measurement of the epithelial thickness showed that invasive carcinoma was significantly different than carcinoma *in situ* ($P = 0.004$) and dysplasia was significantly different than metaplasia or hyperplasia ($P = 0.002$). In addition, nuclei of the cells corresponding to histologic results became more discernible in lesions that were moderate dysplasia or worse compared with lower-grade lesions.

Conclusion: Preliminary data suggest that autofluorescence bronchoscopy–guided OCT imaging of bronchial lesions is technically feasible. OCT may be a promising nonbiopsy tool for *in vivo* imaging of preneoplastic bronchial lesions to study their natural history and the effect of chemopreventive intervention.

Lung cancer is the most common cause of cancer death worldwide, with more than 1.3 million people dying of lung cancer annually (1). The 5-year survival rates after the diagnosis of lung cancer has improved only marginally in the last 3 decades (2). Although early detection and chemoprevention is effective in reducing the incidence and mortality of cancer of the breast, there is considerable skepticism in applying the same cancer control strategy in lung cancer. The most common criticism is the uncertain identity of intraepithelial neoplastic (IEN) lesions and the natural history of these lesions.

There are unique challenges in detecting and treating IEN lesions in the lung compared with other organs. The lung is an internal organ consisting of a complex branching system of conducting airways leading to gas exchange units. Lung cancer consists of four major cell types: squamous cell carcinoma, adenocarcinoma, large cell carcinoma, and neuroendocrine tumors (3). They are preferentially located in different parts of the bronchial tree. For example, squamous cell carcinoma and neuroendocrine tumors are more frequently found in the larger central airways compared with adenocarcinoma, which is more frequently found in the small peripheral airways and lung parenchyma. Autofluorescence bronchoscopy is a major advance to improve detection of preinvasive lesions in the central airways by guiding biopsies (4). It has contributed to improved histopathologic classification and molecular profiling of IEN lesions (5–7). It allows rapid scanning of large areas of the bronchial surface for subtle abnormalities that are not visible to white-light examination. However, the improved sensitivity of autofluorescence bronchoscopy to detect preneoplastic lesions is associated with a decrease in specificity compared with white-light examination due to false-positive fluorescence in areas of inflammation or increase in epithelial thickness (4, 8, 9). Because the histology cannot be predicted from the degree of abnormal fluorescence with certainty, a biopsy is needed for

Authors' Affiliations: [1]Cancer Imaging Department, British Columbia Cancer Agency and the University of British Columbia, Vancouver, British Columbia, Canada; [2]Department of Medical Biophysics, Princess Margaret Hospital, University of Toronto, Toronto, Ontario, Canada; [3]University of Texas Southwestern Medical Center, Dallas, Texas; and [4]Department of Thoracic Oncology and Surgery, International University of Health and Welfare, Mita Hospital, Tokyo, Japan

Received 9/20/07; revised 12/10/07; accepted 12/18/07.

Grant support: NIH-National Cancer Institute grants 1PO1-CA96964 and U01CA96109.

The costs of publication of this article were defrayed in part by the payment of page charges. This article must therefore be hereby marked *advertisement* in accordance with 18 U.S.C. Section 1734 solely to indicate this fact.

Requests for reprints: Stephen Lam, Cancer Imaging Department, British Columbia Cancer Agency, 675 West 10 Avenue, Vancouver, British Columbia, Canada V5Z 1L3. Phone: 604-675-8094; Fax: 604-675-8089; E-mail: slam@bccancer.bc.ca.

doi:10.1158/1078-0432.CCR-07-4418

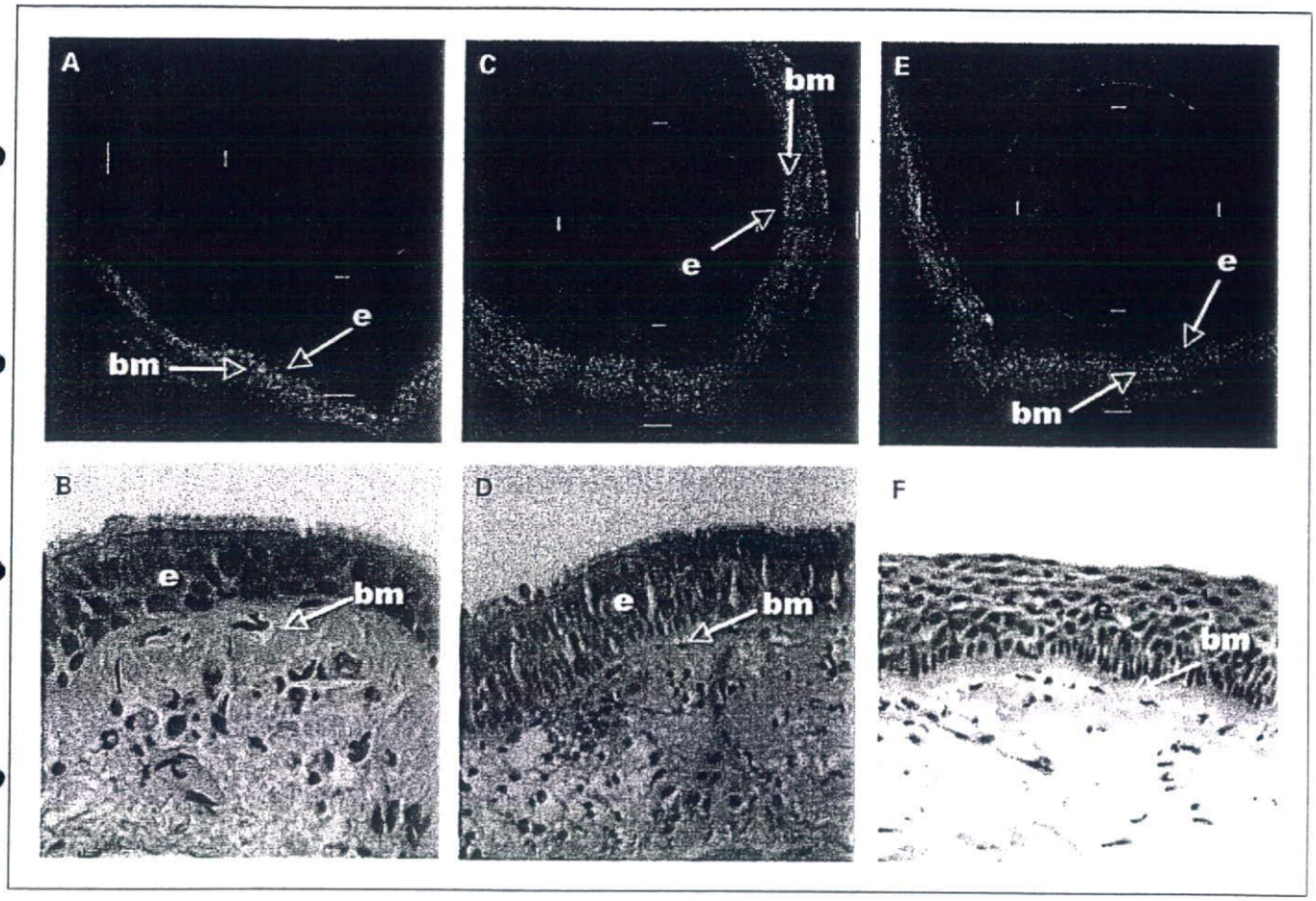

Fig. 1. Representative images of normal healthy human bronchus by standard histologic section (H&E stain; original magnification, ×20; *A*) and OCT (*B*) showing a single-layer epithelium (*e*) on top of the basement membrane (*bm*) and upper submucosa. The basement membrane and upper submucosa are highly reflective due to the presence of collagen. Each calibration mark in the OCT image is equal to 1 mm. *C* and *D*, from an area with hyperplasia. *E* and *F*, from an area with metaplasia.

confirmation. Serial bronchial biopsies are currently used to sample IEN lesions to study the natural history of these lesions and to evaluate the effect of chemopreventive agents in phase II clinical trials (10–15). We have previously reported that 55% of the dysplastic lesions are ≤1.5 mm in size (range, 0.5-1.5 mm; ref. 9). Using careful microdissection and molecular analyses of ~200 cells in contiguous areas of the bronchial epithelium, most of the clonal patches from IEN lesions were found to be very small, containing ~90,000 cells (16). Because the size of a bronchial biopsy forceps is 1.5 mm in diameter, the biopsy procedure itself can potentially remove these lesions mechanically. It is therefore important to develop nonbiopsy methods that can determine the presence and progression/regression of IEN lesions in the bronchial epithelium.

Optical coherence tomography (OCT) is an optical imaging method that can offer microscopic resolution for visualizing cellular and extracellular structures at and below a tissue surface (17–19). In principle, it is similar to ultrasound. Instead of using sound waves, near-IR light is passed into the tissue, and by detecting the reflected light as it interacts with tissue structures as a function of depth, a cross-sectional image is created through optical interferometry. Unlike ultrasound, light waves do not require liquid-based coupling medium and thus are more compatible with airway imaging. There are no associated risks from the weak near-IR light. Preliminary data by one of us (N.I.) suggested that *in situ* and invasive carcinoma can be distinguished from normal bronchial epithelium (20). The intrinsic high spatial resolution of OCT can also become one of its limitations because large amount of data will be accumulated if the entire airway surface is to be imaged at micron-scale resolutions. Autofluorescence bronchoscopy, although lacking the microscopic resolution of OCT, is capable of imaging large portions of the central airway rapidly and may be complementary to OCT.

In the current study, we investigated whether dysplastic lesions and *in situ* carcinoma from high-risk smokers can be distinguished from hyperplasia or metaplasia using OCT. The microscopic OCT imaging is done under the guidance of autofluorescence bronchoscopy. In a large cohort of high-risk heavy smokers, we show for the first time that dysplasia and carcinoma *in situ* (CIS) can be distinguished from lower-grade lesions.

Materials and Methods

Study population and procedures. The study population consisted of participants in two ongoing NIH-National Cancer Institute–sponsored chemoprevention trials (1PO1-CA96964 and U01CA96109). The participants were either current or former smokers ages 45 to 74 y

with a smoking history of ≥30 pack-years. One hundred thirty-eight volunteer smokers, 99 men and 39 women, participated in the study. To determine the differences between CIS and microinvasive/invasive tumors, 10 patients, 7 men and 3 women, undergoing bronchoscopy for diagnosis or treatment of lung cancer were also included into the study. The mean age of the 148 subjects was 62 ± 8 y. Twenty-seven were current smokers and 121 were former smokers. The average smoking intensity was 49 ± 17 pack-years. The study was approved by the Clinical Investigation Committee of the British Columbia Cancer Agency and the University of British Columbia.

White-light and autofluorescence bronchoscopy was done using the Onco-LIFE device (Novadaq Technologies, Inc.) under local anesthesia to the upper airways and conscious sedation as described previously (13–15). Areas suspicious of dysplasia or cancer were noted. Before taking a biopsy, OCT imaging was done by inserting a small optical probe with an outer diameter of 1.5 mm and a depth of focus of 3 mm. The OCT probe was inserted through the biopsy channel of the bronchoscope directly over the site of interest. The OCT image was displayed on a monitor in real time and recorded digitally.

Optical coherence tomography. The OCT system used in the study is a preproduction model, which was developed in a collaboration between LightLab Imaging and Pentax. The design of the system has been described by one of us (N.I.) previously (20). Briefly, low coherence light from a 1,300-nm superluminescent diode source with a bandwidth of 50 nm is split evenly, half toward the bronchial surface via a fiberoptic catheter and half toward a moving mirror. Light is then reflected both from within the tissue and from the mirror. If the distance traveled by light in both arms is nearly identical, interference will occur when the light reflected recombine at the beam splitter. The position of the moving reference arm mirror is precisely controlled electronically. Moving the mirror allows interference (back reflection) information to be obtained from different depths within the sample.

The theoretical axial resolution of the OCT system is 15 to 20 μm. The lateral/transverse resolution is 21 to 27 μm within the appropriate depth of focus (1-2 mm) for bronchial imaging. The position of the focused beam was mechanically scanned across the bronchial luminal surface in 360 degrees at a frame rate of 4 Hz. Axial profiles were digitized for each scan position to create a two-dimensional cross-sectional image.

Correlation of OCT images with pathology of bronchial biopsies. Bronchial biopsies were done in sites with abnormal fluorescence under autofluorescence bronchoscopic guidance as described previously (8, 13–15). Biopsies were also taken from normal control sites as per the chemoprevention trial protocols. The biopsy samples were fixed in buffered formalin, embedded in paraffin, cut into 5 μm sections, and stained with H&E. They were systematically reviewed by two pathologists (J.L. and A.G.) without knowledge of the OCT findings and classified into one of the following eight groups (normal, basal cell hyperplasia, metaplasia, mild/moderate/severe dysplasia, CIS, or invasive carcinoma) according to the WHO criteria (3). Tissue slide examination and micrographs were done with a Nikon Eclipse 80i and recorded with a Nikon digital net camera.

The OCT images were reviewed independently by two scientists (B.S. and S.L.). Normal and abnormal areas were identified. Differences were

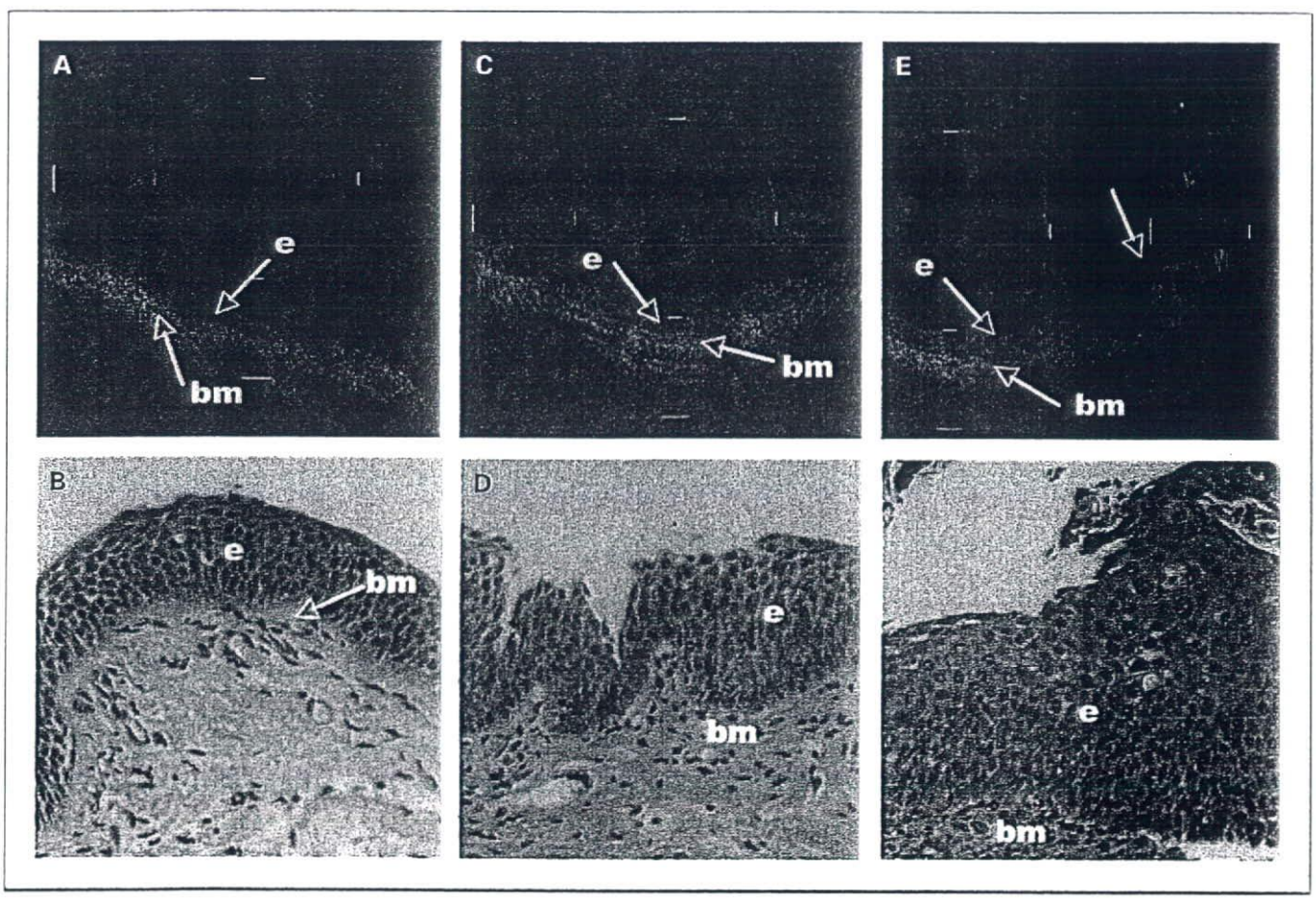

Fig. 2. Representative OCT images of an area with mild dysplasia (*A*), moderate dysplasia (*C*), and severe dysplasia (*E*) and corresponding H&E-stained histologic sections (*B, D,* and *F*; original magnification, ×20). The nuclei in the epithelium become recognizable as darker dots with moderate dysplasia or worse. The arrow in the OCT image of the area with severe dysplasia points to the corresponding elevated area in the H&E section.

resolved by reviewing the images together. The epithelial thickness in the area of interest from the epithelial surface to the basement membrane was quantified by one scientist (B.S.) using ImageJ (Research Services Branch, NIH, Bethesda, MD).

Statistical analysis. The epithelial thickness of the OCT images in different histopathology groups was compared. Normal and hyperplasia were combined into one category for comparison with the higher-grade lesions using the Student's *t* test. All statistical analyses were done using JMP v5.0. All *P* values were two sided and the level of statistical significance was set at $P < 0.05$.

Results

A total of 281 OCT images followed by bronchial biopsy of the same site were taken from the 148 participants. The histopathology of these areas includes 145 normal/hyperplasia, 61 metaplasia, 39 mild dysplasia, 10 moderate dysplasia, 6 severe dysplasia, 7 CIS, and 13 invasive carcinomas. A representative OCT image from each of these seven groups along with the pathology finding is shown in Figs. 1 to 3. Normal or hyperplasia is characterized by one or two cell layers above a highly scattering basement membrane and upper submucosa (Fig. 1). Clear imaging is seen to a depth of ~2 mm to the cartilage layer. As the epithelium changes from normal/hyperplasia to metaplasia, various grades of dysplasia, and CIS, the number of cells in the epithelial layers increases (Figs. 2 and 3). The nuclei became more readily visible in high-grade dysplasia or CIS, although this was at the limit of resolution of the current OCT system. The basement membrane was still intact in CIS (Fig. 3A) but became discontinuous or no longer visible with invasive cancer (Fig. 3C).

The results of the quantitative measurement of the epithelium are shown in Fig. 4. The epithelial thickness was significantly different between invasive cancer and CIS ($P = 0.004$). Severe dysplasia and CIS tended to be thicker than mild or moderate dysplasia but the results did not reach statistical significance ($P = 0.39$). Taken together, mild, moderate, and severe dysplasia were significantly thicker than metaplasia ($P = 0.002$). Mild dysplasia tended to be thicker than metaplasia but the results did not reach statistical significance ($P = 0.069$).

Discussion

The goal of the present study was to establish a library of OCT images with the corresponding pathology finding to determine if OCT can discriminate dysplasia and CIS from normal, hyperplasia, or metaplasia. Our data show that invasive cancer can be distinguished from CIS and that dysplasia can be distinguished from metaplasia, hyperplasia, or normal. Using quantitative measurement, a progressive increase in the epithelial thickness was found to parallel the severity of the histopathology grade. The nuclei of the cells also became more discernible as darker less light scattering objects in lesions that are moderate dysplasia or worse. The basement

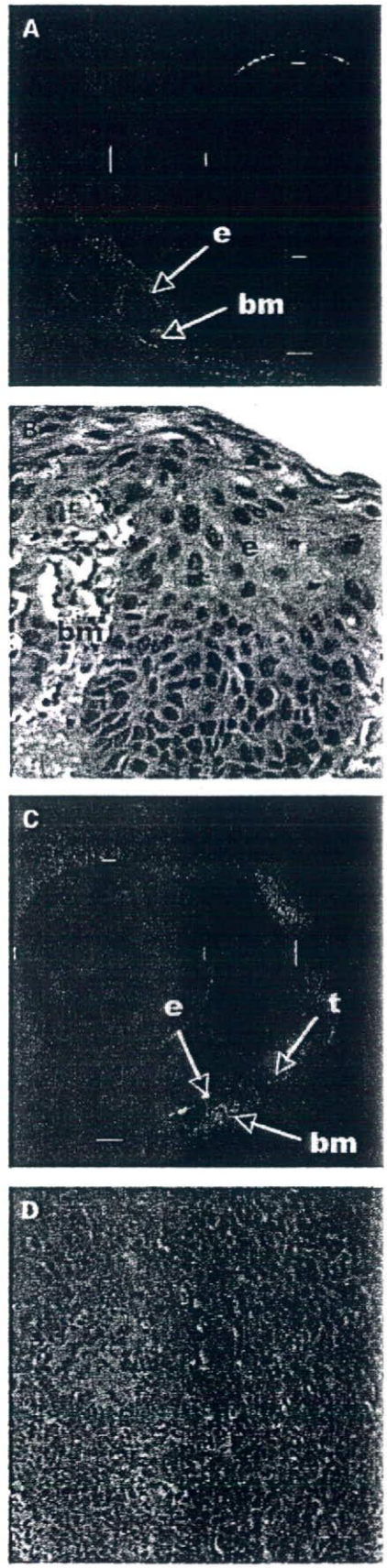

Fig. 3. Representative OCT images of an area with CIS (*A*) and invasive cancer (*C*) and the corresponding H&E-stained histologic section (*B* and *D*; original magnification, ×20). The papillary changes and the enlarged nuclei in the H&E section are clearly recognized in the OCT image as larger, darker, and less scattering dots. For the invasive carcinoma, invasion through the basement membrane in the right lower corner and disappearance of the basement membrane in the upper half of the OCT image can be observed.

membrane became disrupted or disappeared with invasive carcinoma.

There is considerable uncertainty about the natural history of bronchial IEN lesions. Sequential biopsies of the same sites in volunteer smokers with bronchial dysplasia showed a high regression rate at the end of 6 months in those who were in the placebo arm of the chemoprevention trial (13–15). Twenty percent of the current smokers and 50% of the former smokers had complete resolution of their dysplasia to hyperplasia or normal (13–15). Other studies also attempted to clarify the natural history of preneoplastic lesions and CIS using serial bronchoscopy and biopsy (10–12, 21, 22). These studies were relatively small (~50 patients or less). Similar to our shorter-term studies (13–15), >50% of the dysplastic lesions regressed spontaneously on follow-up (8, 10, 11). The extent to which mechanical removal of the dysplastic lesion contributes to the apparently high regression rate of dysplasia is unknown. The high regression rate of bronchial dysplasia complicates the evaluation of chemopreventive agents. A nonbiopsy method would help to clarify the natural history of these lesions and the effect of chemopreventive intervention.

Currently, there are two imaging modalities that have sufficient spatial resolution and tissue depth penetration to study the bronchial epithelial and subepithelial changes associated with lung cancer development. Confocal microendoscopy is an attractive tool as it offers spatial resolution down to the submicron range. However, cells do not emit strong autofluorescence. Although the basement membrane and upper submucosa can be imaged with superb quality, the epithelial cells are not visible (23, 24). In addition, because contact with the bronchial surface is required, the fragile epithelium can be scrapped off during the imaging procedure. Motion artifacts due to cardiac pulsation and respiratory movements can also lead to suboptimal imaging of cellular details. OCT is a noncontact method that delivers near-IR light to the tissue and allows imaging of cellular and extracellular structures from analysis of the back scattered light with a spatial resolution of 4 to 15 μm and a depth penetration of ~2 mm to provide near-histologic images in the bronchial wall (17–20). The fiberoptic probes can be miniaturized to enable imaging of airways down to the terminal bronchiole beyond the range of a standard bronchoscope. The procedure is simple and adds <5 min to a standard bronchoscopic procedure under local anesthesia and conscious sedation. The *in vivo* imaging findings in invasive carcinoma and CIS in the present study are similar to the preliminary study by one of us (N.I.; ref. 20) and the *ex vivo* study by Whiteman et al. (25). We have extended these earlier studies to show that dysplasia (especially high grade) and CIS can be distinguished from lower-grade lesions *in vivo*.

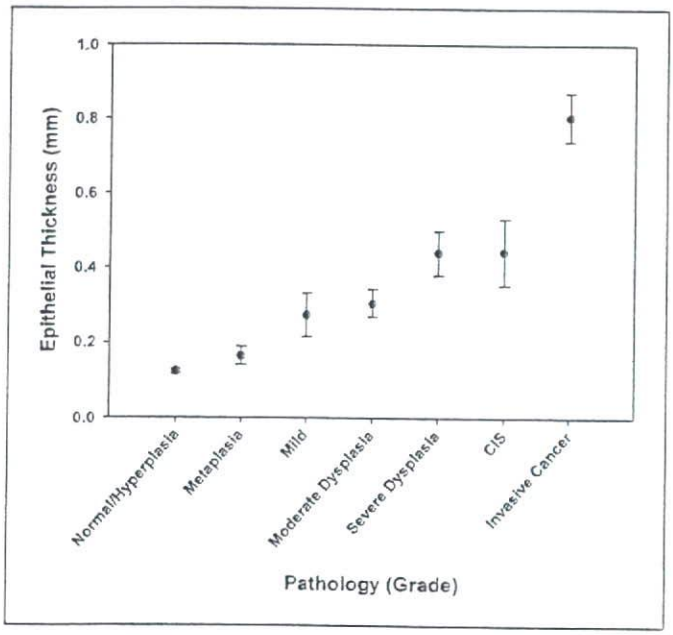

Fig. 4. Quantitative measurements of the epithelium in the OCT images from different histologic grades. There is a progressive increase in the thickness due to a multilayer structure and larger nuclei as the epithelium changes from normal/hyperplasia to metaplasia, mild, moderate, or severe dysplasia, to CIS and invasive carcinoma.

Our study has several important strengths. To our knowledge, this is the first study that combines the large area imaging capability of autofluorescence endoscopy and the microscopic imaging resolution of OCT. Autofluorescence bronchoscopy makes use of fluorescence and absorption properties to provide information about the biochemical composition and metabolic state of bronchial tissues. The fluorescence properties of bronchial tissue are determined by the concentration of the cellular and extracellular fluorophores, their metabolic state, the tissue architecture, and the wavelength-dependent light attenuation due to the concentration as well as distribution of nonfluorescent chromophores such as hemoglobin (3, 26). Collagen and elastin are the most important structural fluorophores. Examples of fluorophores involved in cellular metabolism include NAD^+ and flavins. The autofluorescence yield in the subepithelial tissue is ~10 times higher than the epithelium. As the bronchial epithelium changes from normal to dysplasia, and then to CIS and invasive cancer, there is a progressive decrease in green autofluorescence but proportionately less decrease in red fluorescence intensity. This change is due to a combination of several factors, such as a decrease in the extracellular collagen and elastin, an increase in the number of cell layers associated with dysplasia or cancer, decrease in the fluorescence measured in the bronchial surface due to reabsorption of fluorescent light by a thickened epithelium, increase in absorption of the blue excitation light, and reduced fluorescence due to an increase in the microvascular density/blood volume as well as a reduction in the amount of flavins and NAD^+ in premalignant and malignant cells (3, 26). Because the microvasculature and blood volume is increased in inflammatory lesions and the epithelial thickness is increased with marked goblet cell hyperplasia or metaplasia, false-positive fluorescence can occur in a benign epithelium. Thus, although autofluorescence provides useful information on the biochemical and functional changes in the bronchial epithelium and autofluorescence bronchoscopy serves as a rapid scanning tool to localize preneoplastic and neoplastic lesions, autofluorescence alone cannot be used to study the natural history of these lesions without biopsy confirmation. We systematically examined the changes in the bronchial epithelium associated with the development of squamous cell carcinoma using OCT as a nonbiopsy optical imaging method to provide architectural information in the bronchial epithelium from a large cohort of heavy smokers at risk of developing lung cancer as well as patients with invasive carcinoma. The

multilayer epithelium associated with bronchial dysplasia can be clearly seen. The ability to distinguish dysplasia from lower-grade lesions or inflammation opens the possibility that the effect of chemopreventive agents can be more accurately studied in short-term phase II trials without taking a biopsy before treatment. The same sites can be revisited to document the changes at the end of the treatment period (typically 3-6 months) first by OCT imaging and then by biopsy for histologic confirmation. The spontaneous regression rate of IEN lesions can also be studied in subjects who are treated with placebo. Thus, OCT can complement the rapid scanning ability of autofluorescence bronchoscopy by providing morphologic information to characterize potentially abnormal sites without a biopsy.

Certain limitations to the current study deserve consideration. Different grades of dysplasia could not be distinguished from one another and from CIS using quantitative measurement of the epithelial thickness alone. However, image analysis techniques can be implemented to further investigate the ability of OCT to statistically distinguish different grades of dysplasia from CIS. These techniques include quantifying the SD in OCT signal within a region of interest (27) or texture analysis (28). Architectural measurement of the epithelial changes similar to what has been achieved in morphometric measurements in biopsy specimens (29) may provide an objective grading that is better than the visual grading of the nuclear changes in the present study. Morphometric measurements in OCT images require better spatial resolution than our current OCT device. Systems with higher resolution and Doppler capability that can measure cellular structures in greater detail and quantify vascular density are becoming available for clinical investigation (30, 31). Measurement of second harmonic signal and two-photon excitation coupled with Doppler OCT would further improve the imaging down to the molecular level (32, 33).

In summary, we have shown that autofluorescence endoscopy–guided OCT imaging of bronchial lesions is technically feasible. OCT may be a promising nonbiopsy tool for *in vivo* imaging of preneoplastic bronchial lesions to study their natural history and the effect of chemopreventive agents.

Acknowledgments

We thank Pentax Corp. for providing the OCT device for the study and Myles Mckinnon, Sokhpal Sohi, Edward Mamo, and Sukhinder Khattra for their technical assistance and data management for the study.

References

1. Ezzati M, Lopez AD. Estimates of global mortality attributable to smoking in 2000. Lancet 2003;362:847–52.
2. Jemal A, Siegel R, Ward E, Murray T, Xu J, Thun MJ. Cancer statistics, 2007. CA Cancer J Clin 2007;57:43–66.
3. Travis WD, Colby TV, Corrin B, Shimosato Y, Brambilla E. Histologic and graphical text slides for the histological typing of lung and pleural tumors. In: World Health Organization Pathology Panel: World Health Organization. International classification of tumors. Berlin: Springer Verlag; 1999; p. 5–30.
4. Lam S, McWilliams A. The role of autofluorescence bronchoscopy in diagnosis of early lung cancer. In: Hirsch FR, Bunn Jr PA, Kato H, Mulshine JL, editors. IASLC textbook of prevention and early detection of lung cancer. Taylor and Francis Group UK; 2005; p. 149–60.
5. Wistuba II, Behrens C, Virmani AK, et al. High resolution chromosome 3p allelotyping of human lung cancer and preneoplastic/preinvasive bronchial epithelium reveals multiple, discontinuous sites of 3p allele loss and three regions of frequent breakpoints. Cancer Res 2000;60:1949–60.
6. Garnis C, Davies J, Buys T, et al. Chromosome 5p aberrations and glial cell line-derived neurotrophic factor activation are early events in lung cancer. Oncogene 2005;24:4806–12.
7. Guillaud M, leRiche J, Daw C, et al. Nuclear morphometry as a biomarker for bronchial intraepithelial neoplasia: correlation with genetic damage and cancer development. Cytometry A 2005;63:34–40.
8. Lam S, Kennedy T, Unger M, et al. Localization of bronchial intraepithelial neoplastic lesions by fluorescence bronchoscopy. Chest 1998;113:696–702.
9. Lam S, MacAulay CE, leRiche JC, Palcic B. Detection and localization of early lung cancer by fluorescence bronchoscopy. Cancer 2000;89:2468–73.
10. Breuer RH, Pasic A, Smit EF, et al. The natural course of pre-neoplastic lesions in bronchial epithelium. Clin Cancer Res 2005;15:537–43.
11. Bota S, Auliac JB, Paris C, et al. Follow-up of bronchial precancerous lesions and carcinoma *in situ* using fluorescence endoscopy. Am J Respir Crit Care Med 2001;164:1688–93.
12. Hoshino H, Shibuya K, Chiyo M, et al. Biological features of bronchial squamous dysplasia followed up by autofluorescence bronchoscopy. Lung Cancer 2004;46:187–96.
13. Lam S, MacAulay C, leRiche JC, et al. A randomized phase IIb trial of anethole dithiolethione in smokers with bronchial dysplasia. J Natl Cancer Inst 2002;94:1001–9.
14. Lam S, Xu XC, Parker-Klein H, et al. Surrogate endpoint biomarker analysis in a retinol chemoprevention trial in current and former smokers with bronchial dysplasia. Int J Oncol 2003;23:1607–13.
15. Lam S, leRiche JC, McWilliams A, et al. A randomized phase IIb trial of pulmicort turbuhaler (budesonide) in people with dysplasia of the bronchial epithelium. Clin Cancer Res 2004;10:6502–11.
16. Park IW, Wistuba II, Maitra A, et al. Multiple clonal abnormalities in the bronchial epithelium of patients with lung cancer. J Natl Cancer Inst 1999;91:1863–8.
17. Huang D, Swanson EA, Lin CP, et al. Optical coherence tomography. Science 1991;254:1178–81.
18. Fujimoto JG, Brezinski ME, Tearney GJ, et al. Biomedical imaging and optical biopsy using optical coherence tomography. Nat Med 1995;1:970–2.
19. Tearney GJ, Brezinski ME, Bouma BE, et al. *In vivo* endoscopic optical biopsy with optical coherence tomography. Science 1997;276:2037–9.
20. Tsuboi M, Hayashi A, Ikeda N, et al. Optical coherence tomography in the diagnosis of bronchial lesions. Lung Cancer 2005;49:387–94.
21. Venmans B, van Boxem A, Smit E, Postmus P, Sutedja T. Outcome of bronchial carcinoma *in situ*. Chest 2000;117:1572–6.
22. Weigel TL, Yousem S, Dacic S, Kosco PJ, Siegfried J, Luketich JD. Fluorescence bronchoscopic surveillance after curative surgical resection for non-small-cell lung cancer. Ann Surg Oncol 2000;7:176–80.
23. Thiberville L, Moreno-Swirc S, Vercauteren T, Peltier E, Cave C, Heckly GB. *In vivo* imaging of the bronchial wall microstructure using fibered confocal fluorescence microscopy. Am J Respir Crit Care Med 2007;175:22–31.
24. MacAulay C, Lane P, Richards-Kortum R. *In vivo* pathology: microendoscopy as a new endoscopic imaging modality. In: Van Dam J, editor. Gastrointestinal endoscopy clinics of North America: optical biopsy. Elsevier Netherlands; 2004. p. 595–620.
25. Whiteman SC, Yang Y, van Pittius DG, Stephens M, Parmer J, Spiteri MA. Optical coherence tomography: real-time imaging of bronchial airways microstructure and detection of inflammatory/neoplastic morphological changes. Clin Cancer Res 2006;12:813–8.
26. Wagnieres G, McWilliams A, Lam S. Lung cancer imaging with fluorescence endoscopy. In: Mycek M, Pogue B, editors. Handbook of biomedical fluorescence. New York: Marcel Dekker; 2003. p. 361–96.
27. Tearney GJ, Yabushita H, Houser SL, et al. Quantification of macrophage content in atherosclerotic plaques by optical coherence tomography. Circulation 2003;107:113–9.
28. Qi X, Sivak MV, Isenberg G, Willis JE, Rollins AM. Computer-aided diagnosis of dysplasia in Barrett's esophagus using endoscopic optical coherence tomography. J Biomed Opt 2006;11:044010.
29. Guillaud M, Cox D, Storthz KA, et al. Exploratory analysis of quantitative histopathology of cervical intraepithelial neoplasia: objectivity, reproducibility, malignancy-associated changes, and human papillomavirus. Cytometry A 2004;60:81–9.
30. Yang VXD, Tang S, Gordon ML, et al. Endoscopic Doppler optical coherence tomography in the human GI tract: initial experience. Gastrointest Endosc 2005;61:879–90.
31. Standish BA, Yang VXD, Munce NR, et al. Doppler optical coherence tomography monitoring of microvascular response during photodynamic therapy in a Barrett's esophagus rat model. Gastrointest Endosc 2007;66:326–33.
32. Tang S, Sun CH, Krasieva TB, Chen ZP, Tromberg BJ. Imaging sub-cellular scattering contrast using combined optical coherence and multiphoton microscopy. Opt Lett 2007;32:50305.
33. Tang S, Krasieva TB, Chen ZP, Tromberg BJ. Combined multiphoton microscopy and optical coherence tomography using a 12-fs, broadband source. J Biomed Opt 2006;11:020502.

Disease-Free Interval Length Correlates to Prognosis of Patients Who Underwent Metastasectomy for Esophageal Lung Metastases

Satoshi Shiono, MD, Masafumi Kawamura, MD,† Toru Sato, MD,* Ken Nakagawa, MD,‡ Jun Nakajima, MD,§ Ichiro Yoshino, MD,‖ Norihiko Ikeda, MD,¶ Hirotoshi Horio, MD,# Hirohiko Akiyama, MD,** and Koichi Kobayashi, MD†; The Metastatic Lung Tumor Study Group of Japan*

Background: Pulmonary metastasectomy is a standard method for treatment of selected pulmonary metastases cases. Nevertheless, because prognosis for patients with lung metastases from esophageal cancer who have undergone pulmonary metastasectomy is poor, candidates for this method of treatment are rare. Therefore, the efficacy of surgical treatment for pulmonary metastatic lesions from esophageal cancer has not been thoroughly examined.

Methods: Between March 1984 and May 2006, 57 patients underwent resection of pulmonary metastases from primary esophageal cancer. These cases were registered in the database developed by the Metastatic Lung Tumor Study Group of Japan and were retrospectively reviewed from the registry. After excluding eight cases because of missing information, we reviewed the remaining 49 cases and examined the prognostic factors for pulmonary metastasectomy for metastases from esophageal cancer.

Results: There were no perioperative deaths. After pulmonary metastasectomy, disease recurred in 16 (33%) of the 49 patients. The overall 5-year survival was 29.6%. Median survival time was 18 months. The survival of patients with a disease-free interval (DFI) less than 12 months was significantly lower than patients with a DFI greater than 12 months. Through multivariate analysis, we identified DFI as a clinical factor significantly related to overall survival ($p = 0.04$).

Conclusions: We identified that patients with a DFI less than 12 months who underwent pulmonary metastasectomy for metastases from esophageal cancer had a worse prognosis. Pulmonary metastasectomy for esophageal cancer should be considered for selected patients with a DFI ≥12 months.

Key Words: Esophageal cancer, Pulmonary metastasis, Metastasectomy.

(*J Thorac Oncol.* 2008;3: 1046–1049)

Pulmonary metastasectomy is a standard method of treatment for selected pulmonary metastases cases.[1] When patients are appropriately selected for this treatment, the overall 5-year survival after pulmonary metastasectomy is about 30 to 40%.[1,2] In general, because prognosis for patients who have undergone this method of treatment is poor with disease frequently recurring, pulmonary metastasectomy is not a frequently chosen method of treatment for lung metastases from esophageal cancer. Consequently, survival after surgery for pulmonary metastases from esophageal cancer has not been thoroughly examined. In Japan, the annual report by the Japanese Association for Thoracic Surgery does not document patients who underwent metastasectomy for metastasized esophageal cancer.[3] Because the outcome of pulmonary metastasectomy for metastases from esophageal cancer has not been thoroughly investigated, it is controversial whether surgery is an effective treatment for metastatic esophageal cancer. To identify prognostic factors of pulmonary metastasectomy for metastases from esophageal cancer, in the present study, we reviewed cases registered in the Metastatic Lung Tumor Study Group of Japan database of patients who underwent metastasectomy for metastasized esophageal cancer.

PATIENTS AND METHODS

The Metastatic Lung Tumor Study Group of Japan developed a database for registration of lung metastases cases. These patients all underwent surgical resection. The database documents the following parameters: gender; age; histology; status of the primary tumor; treatment for the primary tumor; date of primary surgery; kind of surgery; curability; date of metastasis; disease-free interval (DFI); side, size and numbers of resected metastases; date of metas-

*Department of Thoracic Surgery, Yamagata Prefectural Central Hospital, Yamagata, Japan; †Department of Thoracic Surgery, Keio University School of Medicine; ‡Department of Chest Surgery, Cancer Institute Hospital; §Department of Cardiothoracic Surgery, University of Tokyo, Tokyo, Japan; ‖Department of Thoracic Surgery, Chiba University, Chiba, Japan; ¶Department of First Surgery, Tokyo Medical University; #Department of General Thoracic Surgery, Tokyo Metropolitan Komagome Hospital, Tokyo, Japan; and **Department of Thoracic Surgery, Saitama Cancer Center, Saitama, Japan.

Disclosure: The authors declare no conflict of interest.

Address for correspondence: Satoshi Shiono, MD, Department of Thoracic Surgery, Yamagata Prefectural Central Hospital, 1800, Oazaaoyagi, Yamagata 990-2292, Japan. E-mail: sshiono@ypch.gr.jp

ISSN: 1556-0864/08/0309-1046